

Cancer as Boundary Logic Failure

A Computational and Information-Theoretic Framework
for the Internal Self-Referential Malignancy

Moses Rahnama

Mina Analytics

moses@minaanalytics.com

February 2026

Abstract. We propose a boundary-first framework for cancer: malignancy emerges when organism-level termination predicates weaken and cells enter a self-referential proliferative loop. In this view, cancer is a boundary-logic failure in cross-scale observability and control, not only a catalog of molecular lesions. We model unbounded proliferation as structurally analogous to recursive self-duplication without a halt predicate, link metabolic expansion (Warburg effect) and cachexia to a “budget escape” that violates homeostatic resource constraints, and derive “forced distinction” as a unifying therapeutic design principle spanning checkpoint inhibition, differentiation therapy, bioelectric recoupling, and chronotherapy. The framework identifies two mechanistically distinct boundary-failure modes: Active Masking (immune-visible but checkpoint-vetoed) and Temporal Decoherence (immune-invisible through antigen-presentation loss). Thermodynamic information bounds serve as organizing constraints on distinction and record formation, treated as conceptual lower limits rather than direct metabolic estimates.

We evaluate the framework using TCGA bulk RNA-seq and clinical data across six cohorts ($n = 3,611$ tumors; $n = 3,920$ total samples including normals). Across all six cohorts, circadian CV (a within-sample six-gene clock-structure dispersion proxy) is negatively associated with PD-L1 (CD274), with FDR-significant effects in every cohort ($\rho = -0.125$ to -0.381 , all $q < 0.05$). Tumors show lower circadian CV than matched normals in 4/5 cancer types, consistent with transcriptional clock restructuring (“locked, not broken”). Boundary-failure subtype analysis shows one FDR-significant survival endpoint after BH correction across all 12 pre-specified cohort-level tests: melanoma (log-rank $p = 0.0011$, $q = 0.0132$); lung adenocarcinoma is nominal only ($p = 0.049$, $q = 0.294$); remaining tests are non-significant.

Sensitivity analyses support robustness of the melanoma signal (threshold sweep significant at 9/11 percentiles; RMST difference at 120 months: +24.2 months, 95% CI 10.8 to 36.8) and show that the circadian-checkpoint coupling persists after immune-fraction residualization and purity stratification. An independently constructed observability index (orthogonal to the subtype definition) separates Active Masking from Decoherence at $p < 10^{-10}$. External replication in an independent nivolumab melanoma cohort (GSE91061, $n = 49$ pre-treatment) reproduces the correlation direction ($\rho = -0.283$, $p = 0.049$), while subtype-level response comparison is underpowered. These results support a falsifiable, non-clinical failure-mode framework with explicit positive, nominal, and null evidence boundaries.

Contents

1	Introduction	4
2	The Necessary Bug: Mutation as the Price of Innovation	5
3	Positioning Within Cancer Theory	6
4	Boundary Failure as Loss of Cross-Scale Observability	8
4.1	Relational Identity and Organism-Level Control	8
4.2	The Identity Collapse	8
4.3	Distinctness, Information, and Energetic Constraints	8
5	A Structural Analogy to Recursive Self-Duplication	9
5.1	The Computational Pattern	9
5.2	The Biological Reading (Analogy, Not Identity)	10
5.3	Why the Analogy Is Useful	10
6	A Control-Budget Formulation of Metabolic Escape	11
7	Temporal Coordination and Loss of Synchrony	13
7.1	Circadian Disruption and Cancer	13
7.2	Loss of Temporal Coordination as Boundary Failure	13
7.3	Perineural Invasion Reinterpreted	14
8	Immune Evasion as Loss of Distinguishability	14
8.1	The PD-1/PD-L1 Checkpoint Axis	14
8.2	Secondary Boundary Failures	15
8.3	Gap Junctions and Antigen Broadcast	15
9	Thermodynamic Perspective: Cost Externalization	15
9.1	The Warburg Effect as Metabolic Decoupling	15
9.2	Cachexia as Systemic Cost Payment	15
9.3	Entropy Production (Heuristic)	16
10	Toy Formalism: Tissue as a Labeled Graph	16
10.1	State Variables	16
10.2	A Coherence Metric	17
10.3	Cancer Transform Operator	17
11	Toward Measurable Proxies	18
12	Therapeutic Design Principle: Restore Observability and Enforce Termination	18
12.1	Force Distinction	19
12.2	Restore Termination Predicates	19
12.3	Re-couple to Tissue Constraints	19

12.4 Constrain Resource Externalization	19
13 Clinical Correlations and Testable Hypotheses	20
14 Empirical Validation: TCGA Cohort Analysis	21
14.1 Circadian Coherence and PD-L1	21
14.2 PD-L1 and MHC Class I Co-regulation	23
14.3 Gap Junction Expression	24
14.4 Summary of Key Correlations	24
14.5 Tumor vs. Matched Normal Tissue	27
14.6 Active Masking vs. Temporal Decoherence Classification	29
14.7 Survival Analysis	32
14.8 Robustness to Clinical Covariates and Interaction Structure	35
14.9 Stage-Stratified Analysis	38
14.10 Stromal Confound Sensitivity	39
14.11 Composite Observability Index	41
14.12 External Validation: GSE91061 (Nivolumab Melanoma)	42
14.13 Implications for the Framework	43
15 Simulation	44
15.1 Update Rules	44
15.2 What the Simulation Demonstrates	45
16 Limitations	52
17 Conclusion	54
18 Future Research Directions	55
A Code Availability and Reproducibility Assets	60

1 Introduction

Cancer research has often focused on mutation accumulation and pathway deregulation [1, 2]. This work has identified key oncogenes and tumor suppressors, but it can frame cancer as a set of local errors rather than a systemic failure of biological control. We propose a boundary framework: cancer is a logic failure in multicellular boundary management, with a shift from cooperative coordination to self-referential isolation.

We define this state as a **boundary logic failure**: a condition where a local system (the cell) loses informational coupling with the global structure (the organism) and enters a self-referential loop of unbounded proliferation. This framework unifies three distinct physical and mathematical domains into a single conceptual model of malignancy:

1. **Computability Theory:** We model uncontrolled proliferation as a structural analogy to the recursive successor (`rec_succ`) pattern, a process where the “step” instruction is duplicated in the recursive call without a strong external termination predicate [11, 12].
2. **Thermodynamics and Information Theory:** We apply Landauer’s principle [7] interpretively to cellular division. Normal differentiation involves creating a new informational identity (different gene expression profile, different surface markers, different tissue role). Cancer cells can replicate physical structure while decoupling from organism-level identity constraints, expanding metabolic capacity to sustain proliferative burden and externalizing the cost as systemic metabolic stress and cachexia [32].
3. **Systems Biology:** We reinterpret tumor suppressors as termination predicates in a biological decision process, and frame tissue coherence as a quantifiable metric of cross-scale coupling.

This paper models cancer as a predictable failure mode in systems capable of self-reference and innovation. Framing malignancy as an information problem yields qualitative definitions of tissue coherence and a therapeutic design principle based on “forced distinction”.

Scope and Non-Goals

This is not a molecular or clinical oncology model. It does not predict patient outcomes, infer driver mutations, or reproduce tumor heterogeneity from first principles. It is a failure-mode framework that links self-referential, growth-permissive dynamics to known biology and candidate therapeutic strategies.

Clinical Impact: Boundary-Failure Mode Associates with Survival

The framework is not purely theoretical. Analysis of $n = 3,611$ tumor samples across six TCGA cohorts, plus a deduplicated patient-level survival cohort ($n = 3,089$ with valid overall-survival data), shows that boundary-failure mode is clinically associated with outcome. Figure 1 summarizes FDR-adjusted survival evidence across all cohorts using BH correction across all 12 survival tests: Active Masking vs. Decoherence is significant in melanoma (log-rank $p = 0.0011$, BH $q = 0.0132$), directionally similar but nominal in lung adenocarcinoma

($p = 0.049$, $q = 0.294$), the remaining four AM-vs-DC cohort tests are non-significant, and quartile-based circadian CV alone is non-significant in all six cohorts. Full Kaplan-Meier curves are presented in Section 14.

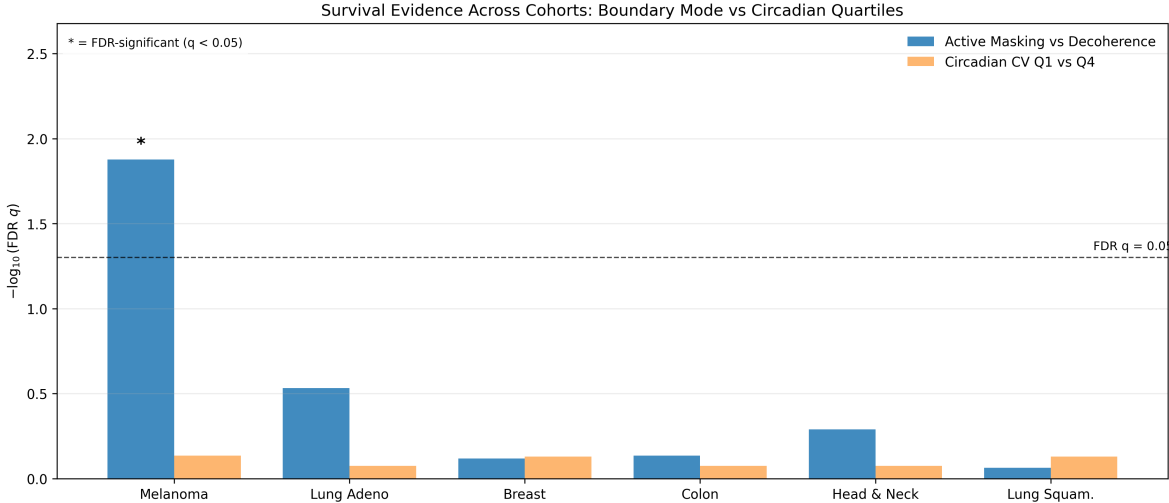


Figure 1: **Cross-cohort survival evidence summary (FDR-adjusted).** Grouped bars show $-\log_{10}(q)$ across six TCGA cohorts for two pre-specified survival tests: Active Masking vs. Decoherence and circadian-CV quartile (Q1 vs Q4), with BH correction across all 12 survival tests. The AM-vs-DC contrast shows strongest support in melanoma (SKCM), while circadian quartiles alone are non-significant across cohorts. In cohorts where both bars remain below the FDR threshold (for example BRCA and LUSC), small bar-order differences are descriptive and not inferential. Asterisks denote FDR-significant tests ($q < 0.05$).

2 The Necessary Bug: Mutation as the Price of Innovation

The central claim of this manuscript is evolutionary before it is clinical: the mechanism that enables adaptation also creates the possibility of malignancy. A living lineage must generate variation to explore new phenotypes under changing environments. Without mutation (sequence variation, recombination, epigenetic drift, and related sources of novelty), evolution cannot “compute” the next viable state.

This creates a structural tension. Let z_t denote the local cellular program and m_t a variation operator. Innovation requires iterative update:

$$z_{t+1} = F(z_t, m_t). \quad (1)$$

In multicellular organisms, this iteration is normally constrained by organism-level termination predicates (checkpoints, differentiation commitments, apoptosis, immune clearance). Healthy adaptation therefore follows:

$$\text{Variation} \rightarrow \text{Selection/Constraint} \rightarrow \text{Termination of unfit trajectories}. \quad (2)$$

Cancer appears when the update channel remains active but the termination channel is weakened or bypassed. The same innovation machinery then amplifies self-preserving local trajectories instead of organism-compatible ones. This is the “necessary bug”: mutation cannot be removed without destroying adaptation, so the therapeutic target is not variation itself but restoration of boundary observability and termination enforcement.

This interpretation is consistent with atavistic perspectives [4] while extending them: the system can rediscover ancestral proliferative programs and also evolve genuinely new resistance strategies because the search loop remains active once boundary control fails.

3 Positioning Within Cancer Theory

A long oncology tradition treats cancer as breakdown of multicellular cooperation. Core perspectives include clonal evolution [3], hallmarks frameworks [1, 2], and multi-scale control failure (checkpoints, contact inhibition [15], immune recognition, and microenvironmental constraints). Tissue organization field theory (TOFT) [6] emphasizes tissue-level causation, showing that stromal disruption can drive aberrant epithelial behavior without requiring epithelial mutations.

Davies and Lineweaver [4] proposed an atavistic model: cancer reverts toward ancestral unicellular phenotypes. Phylostratigraphic evidence supports this shift, with tumors over-expressing older genes and suppressing genes of multicellular origin [5]. In this view, cancer often reactivates ancient programs that multicellular regulation usually constrains.

Our thesis is compatible with these views and uses a unifying language of *observability* and *cross-scale coupling*. Here, *boundary* means the operational separation between what a cell can do and what the organism permits. A healthy boundary is enforced by signals external to each cell that can override local replication programs.

The framework also connects to Levin’s bioelectric work [16, 17]. Cells use ion channels and gap junctions to maintain voltage gradients that encode collective identity. When this integration fails, cells can shift toward unicellular replicative goals. Experimental hyperpolarization can suppress tumor formation despite strong oncogenic drivers [17], which supports the boundary-control interpretation.

The atavistic model explains reactivation of proliferative drives, but critics note that tumors also show neomorphic traits, including drug resistance, that ancestral unicells did not exhibit. In our framework, this follows from loss of termination predicates: once boundary control weakens, the system enters an unbounded search loop. That loop can recover ancestral solutions and also discover new resistance strategies under modern constraints. Cancer is atavistic in origin but evolutionary in progression.

Cancer immunoediting [45, 46] provides the immune-specific counterpart. The “Three Es” framework (Elimination, Equilibrium, Escape) describes how tumors evolve under immune pressure. In our boundary-failure language, the Elimination phase corresponds to intact boundary enforcement; Equilibrium corresponds to a regime where boundary observability is degraded but not yet collapsed; and Escape corresponds to full boundary failure. The Active Masking subtype identified in this paper (Section 14.6) maps to a specific Escape mechanism: the tumor remains antigen-visible but vetoes clearance via checkpoint engagement. The Decoherence subtype represents a distinct Escape route: loss of antigen presentation and

temporal coordination renders the tumor effectively invisible. The boundary framework thus refines the Escape phase into mechanistically distinguishable subtypes with different therapeutic implications.

Preview: Empirical Validation Across Six Cancer Types

Before developing the formal framework, we preview the empirical foundation: validation across six TCGA cancer cohorts ($n = 3,611$ tumor samples) confirms the framework's core predictions. Figure 2 shows a consistent negative circadian CV–PD-L1 coupling in **all six cancer types** (100% replication rate, all FDR-corrected $q < 0.05$): higher PD-L1 is associated with lower circadian CV (more locked/coherent clock-gene expression). This cross-cancer coupling between temporal boundary mechanisms (circadian program state) and immune boundary mechanisms (checkpoint engagement) supports the unifying boundary-failure interpretation. Detailed analysis, survival outcomes, and Active Masking vs. Decoherence stratification are presented in Section 14.

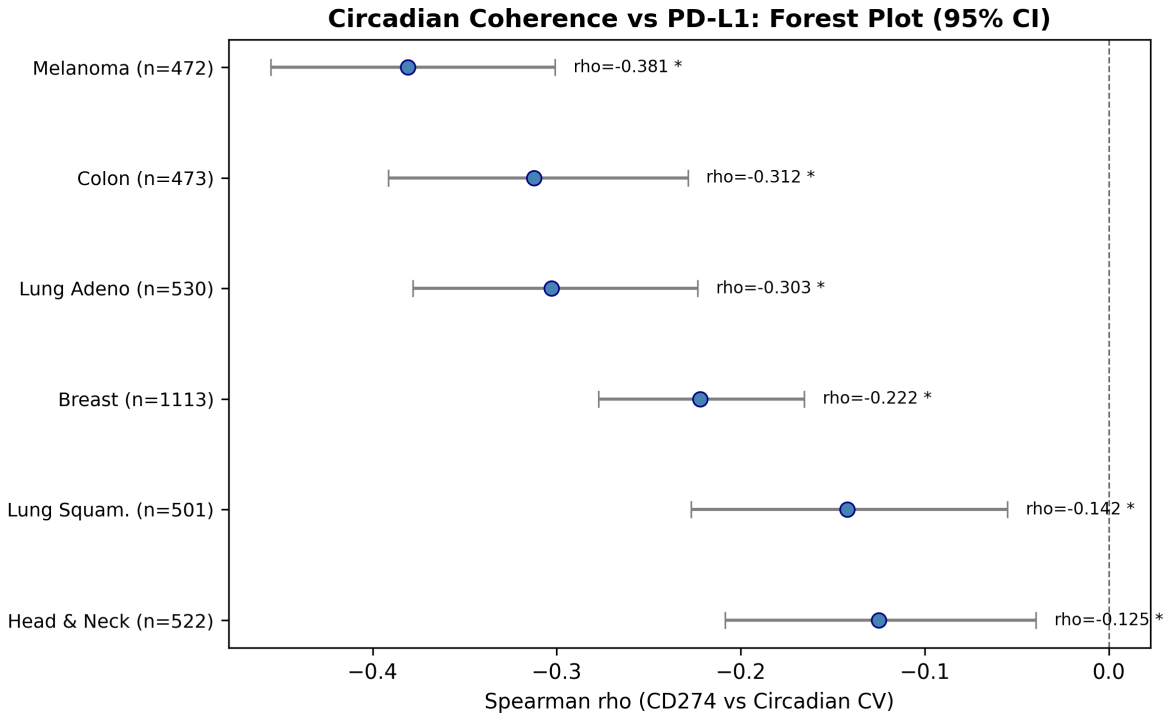


Figure 2: Cross-cancer circadian-CV vs. PD-L1 replication. Forest plot of Spearman correlations for circadian CV versus CD274 across six TCGA cohorts ($n = 3,611$ tumors total). All six effects are negative and FDR-significant, with cohort-specific magnitudes from $\rho = -0.125$ to $\rho = -0.381$. Asterisks (*) denote FDR-significant correlations ($q < 0.05$).

4 Boundary Failure as Loss of Cross-Scale Observability

4.1 Relational Identity and Organism-Level Control

In a multicellular organism, a cell’s “identity” is both intrinsic (gene expression state) and relational: it is stabilized by continuous interaction with surrounding tissue and organism-level regulators. In simplified terms, a healthy cell behaves as if it continuously answers a question of the form:

Am I still operating within the organism’s allowed boundary conditions?

When the answer is “no” (or uncertain), the organism provides termination mechanisms: growth arrest, differentiation cues, senescence, apoptosis [13, 14], and immune-mediated clearance [27]. In this framework, when these mechanisms fail simultaneously, the cell reverts to its most primitive program: divide.

4.2 The Identity Collapse

We model this transition with weighted control allocation. Let $w_{\text{self}}(t)$ and $w_{\text{org}}(t)$ denote the relative influence of cell-autonomous programs and organism-level constraints on cellular decisions at time t , with:

$$w_{\text{self}}(t) + w_{\text{org}}(t) = 1, \quad 0 \leq w_{\text{self}}, w_{\text{org}} \leq 1. \quad (3)$$

Define an alignment index:

$$A(t) = w_{\text{org}}(t) - w_{\text{self}}(t), \quad (4)$$

where healthy tissue corresponds to $A(t) > 0$ (organism-dominant control).

Cancer represents a shift toward self-dominant control ($A(t) \leq 0$), with behavior approaching a closed local decision loop:

$$R_{\text{cell}}^{(t+1)} \approx f(R_{\text{cell}}^{(t)}), \quad \frac{\partial R_{\text{cell}}^{(t+1)}}{\partial u_{\text{org}}^{(t)}} \approx 0, \quad (5)$$

where u_{org} denotes organism-level regulatory input.

In this regime, organism-level signals are present but underweighted. The decision process becomes self-referential. This matches the atavistic view [4]: the cell shifts from multicellular cooperation (“I am part of the organism”) to unicellular survival (“I am the organism”).

4.3 Distinction, Information, and Energetic Constraints

The framework uses “distinction” as an organizing concept: for the organism to control a cell, the cell must be distinguishable in ways that matter for regulation (state, location, lineage, antigen presentation, and response to signals). Maintaining, transmitting, and acting on such distinctions has costs in physical systems [7, 8, 9].

To make this thermodynamic claim explicit without overreach, we use the conditional record-formation lower bound from the boundary-measurement framework [10]. Landauer’s principle has been experimentally verified at the single-bit level [48]; we adopt it here as an organizing principle for biological distinction costs, not as a direct metabolic predictor:

$$\langle Q_{\text{rec}} \rangle \geq k_B T \ln 2 \cdot I(X; Y), \quad (6)$$

where $I(X; Y)$ is classical mutual information between input label X and durable record Y . In biological terms, X can denote antigenic, transcriptional, and context signals, and Y can denote a stable organism-level decision record (tolerate/clear, differentiate/terminate). This is a lower bound on record formation, not a direct estimate of full tumor metabolism.

We adopt a conservative thermodynamic stance: cancer does not evade physical energy costs of replication and signaling. DNA replication consumes ATP; mitosis is energetically expensive. Rather, malignancy can decouple from organism-level identity-establishing processes and degrade the semantic content of distinctions required for regulation, while expanding metabolic capacity to sustain both proliferation and internal coherence. Specifically:

- **Normal differentiation:** The daughter cell acquires a new informational identity (different gene expression profile, different surface markers, different tissue role). This is a semantic distinction that enables immune recognition and tissue coordination.
- **Malignant duplication:** The daughter cell can remain *insufficiently distinguishable* from the parent for reliable organism-level control. The physical replication cost is paid, but the cost of stable identity-bearing differentiation is often externalized to the host. Distinction signals can remain (e.g., neoantigens), yet effective visibility can fall below immune decision criteria when evasion programs (PD-L1 upregulation, MHC-I loss) suppress signal quality.

In later sections we use this to interpret metabolic reprogramming [29, 30] and cachexia [32, 33] via three coupled processes: metabolic expansion (Warburg), direct host resource burden, and tumor-immune inflammatory catabolism.

5 A Structural Analogy to Recursive Self-Duplication

5.1 The Computational Pattern

In a minimal rewrite calculus, a successor-recursion rule has the schematic form:

$$\text{rec}(b, s, \sigma(n)) \rightarrow F(s, \text{rec}(b, s, n)), \quad (7)$$

where b is a base case, s is a step argument, and σ is a successor constructor. In operator-only systems that support ordered computation, the step argument typically reappears in both the outer function application and the recursive call, creating a self-reference that defeats naive additive termination measures when s is unrestricted.

Minimal operator-only rewrite systems formalize this termination pressure and show strong normalization only for guarded fragments; unguarded settings contain the same kind of step-argument redistribution that resists “internal” termination proofs. In that system class, the two recursion rules are:

- $R_{\text{rec_zero}}: \text{rec}_\Delta(b, s, \text{void}) \rightarrow b$ (base case: halt)
- $R_{\text{rec_succ}}: \text{rec}_\Delta(b, s, \delta(n)) \rightarrow \text{app}(s, \text{rec}_\Delta(b, s, n))$ (recursive step)

The critical structure of $R_{\text{rec_succ}}$: the step argument s appears once on the left and is redistributed on the right, once in the outer application and once in the recursive call. When s is itself a recursive term, the system expands without bound.

5.2 The Biological Reading (Analogy, Not Identity)

We use `rec_succ` as a *structural analogy* for malignancy. A healthy tissue contains termination predicates: contact inhibition [15], checkpoints (p53 [13, 14]), and organism-level stop signals. A cancerous process, in contrast, behaves as if the base case has been disabled and the step rule “duplicate and recurse” has become unconditional.

This is a category-level structural analogy, not a claim of formal computational equivalence. Biological processes are stochastic, interruptible, and physically constrained. When termination predicates weaken, the default local dynamic is iterative duplication, and the burden of halting shifts to external regulators (immune surveillance, microenvironmental constraints, therapy).

Computational Domain	Biological Domain	Failure Mode
Function: <code>rec_succ</code>	Process: Mitosis	Unbounded recursion
Operation: $s \rightarrow F(s, \text{rec}(\dots))$	Operation: Cell \rightarrow (Cell, Cell')	Duplication without distinction
Base case: if proven: halt	Base case: Apoptosis / quiescence	Termination predicate lost
Termination check: Measure function	Termination check: p53, checkpoints	Observer cannot verify
Result: Infinite expansion	Result: Tumor growth	System destabilization
Resolution: Accept undecidability; halt	Resolution: Force distinction	Restore observability

Table 1: Structural analogy between `rec_succ` and cancer. This is an analogy about shared failure modes (duplication without termination), not a claim that tumors obey rewrite rules.

5.3 Why the Analogy Is Useful

The `rec_succ` framing clarifies three things that the standard mutation-accumulation model does not emphasize:

1. **Default behavior:** In the absence of active constraints, proliferation is the default, not an acquired capability. This follows the TOFT premise that proliferation is the default state of cells [6]. Mitogenic-induction frameworks place stronger weight on active growth signaling; in that language, the same claim is that once induction barriers are persistently lifted, proliferation becomes the de facto trajectory.

2. **Insufficient distinguishability as the core problem:** The immune system cannot reliably halt what it cannot distinguish above action criteria, just as a termination proof fails when recursive states cannot be separated well enough to certify halt conditions.
3. **The burden of proof shifts:** Halting is not the cell’s responsibility; it is the organism’s. When the organism loses the ability to verify termination (immune evasion, checkpoint loss), the default loop runs.

The evolutionary rationale for why this failure mode exists is developed in Section 2. Here, `rec_succ` is used only as a structural lens: once strong termination predicates are weakened, the duplicate-and-recurse dynamic dominates.

6 A Control-Budget Formulation of Metabolic Escape

To avoid pseudo-fundamental notation, we frame the energetic relationship between proliferation and coherence as a control allocation problem. Let G denote proliferative throughput and S denote maintained tissue coherence (differentiation, signaling, temporal order). Let $C_G(G)$ and $C_S(S)$ be the metabolic and regulatory costs required to sustain these states. Normal homeostasis operates under a bounded budget $B_{\text{homeostasis}}$:

$$C_G(G) + C_S(S) \leq B_{\text{homeostasis}}. \quad (8)$$

In healthy tissue, this creates a necessary trade-off: high proliferation (e.g., during wound healing) temporarily reduces the budget available for complex differentiation, and vice versa.

However, empirical analysis of TCGA cohorts (Section 14) reveals a positive correlation between proliferation and coherence markers in many tumor types, contradicting a simple closed-system trade-off within the tumor. This suggests that malignancy is not merely a reallocation of a fixed budget, but a **budget escape**:

$$C_G(G_{\text{tumor}}) + C_S(S_{\text{tumor}}) > B_{\text{homeostasis}}. \quad (9)$$

The tumor sustains both high proliferation and high internal coherence (the “Active Masking” phenotype) by expanding its metabolic capacity via the Warburg effect and externalizing costs to the host. This interpretation aligns with the cachexia model: the “impossible” high-energy state of the tumor is paid for by systemic catabolism of host tissue.

Control Budget: Pareto Frontier Test
n=3611, p=0.094, boundary slope=0.04

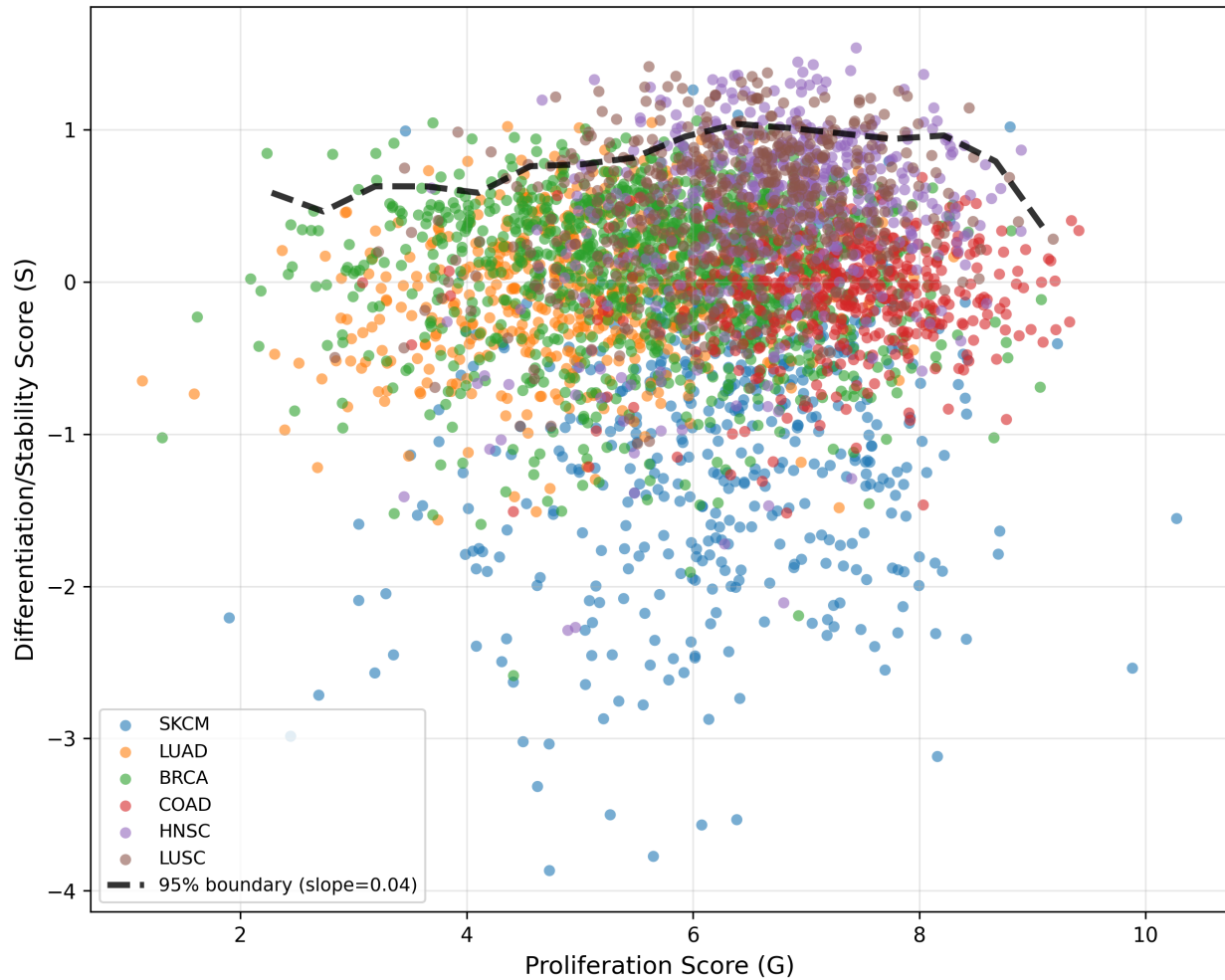


Figure 3: Empirical control-budget stress test across six TCGA cohorts. Proliferation proxy (MYC) is plotted against a composite differentiation/coherence score with upper-bound trend overlays. The absence of a consistent negative frontier supports the manuscript's “budget escape” interpretation rather than a strict in-tumor trade-off.

Property	Normal Tissue Regime	Malignant Regime
Proliferative throughput (G)	Bounded/context-appropriate	Elevated/persistent
Coherence maintenance (S)	High	Variable (can be high in Active Masking)
Budget relation	$C_G + C_S \leq B_{\text{homeostasis}}$ (maintained)	$C_G + C_S > B_{\text{homeostasis}}$ (violation)
Source of excess capacity	N/A	Host catabolism (Cachexia) / Warburg

Table 2: Control-budget view: Cancer as a metabolic violation of homeostatic limits.

Cancer cells do not evade thermodynamics; they redistribute burden across scales. The local ability to sustain high proliferation *without* sacrificing internal coherence (as seen in Active Masking) implies a massive energy draw, which is coupled to increased host-level energetic/inflammatory cost (cachexia).

7 Temporal Coordination and Loss of Synchrony

Many regulatory signals in organisms are time-structured: circadian rhythms, hormonal cycles, metabolic oscillations, and immune rhythms. Healthy tissue can be characterized as *synchronized* to shared temporal references, while malignant regions behave as increasingly *asynchronous*.

7.1 Circadian Disruption and Cancer

The International Agency for Research on Cancer (IARC) has classified night shift work involving circadian disruption as a probable human carcinogen (Group 2A) [20]. Prospective cohort studies of nurses show elevated breast cancer risk after 20+ years of rotating night shifts (RR = 1.79; 95% CI 1.06–3.01) [21]. Finnish twin cohort studies show HR = 1.58 (95% CI 1.16–2.15) for breast cancer among night shift workers, with the critical factor being circadian disruption specifically, not shift work per se [22].

At the molecular scale, core clock components CLOCK and BMAL1 have tumor-suppressive roles: BMAL1 activates ATM signaling for G2/M arrest in colorectal cancer, and the CLOCK-BMAL1 heterodimer suppresses c-Myc-mediated Cyclin E activation in melanoma and colorectal models [23]. Cancer cells often dysregulate these programs. Genetic ablation of BMAL1 promotes lung tumorigenesis by increasing c-Myc activity and glutamine use [23]. Distant tumors can also rewire circadian metabolism in other organs; lung adenocarcinoma alters hepatic STAT3-Socs3 signaling without changing core liver clock genes [24].

7.2 Loss of Temporal Coordination as Boundary Failure

In our framework, temporal coordination is represented by explicit temporal coupling between cells and systemic regulators. “Temporal decoherence” means loss of synchrony in

these couplings, not a claim about literal quantum coherence *in vivo*. Cancer cells decouple from the organism’s temporal regulators and create their own accelerated proliferative cycle, “phasing out” of the organism’s coordinated physiology.

This framing avoids the over-specificity of claiming that cancer requires literal neural disconnection. Many tissues are weakly innervated yet show strong circadian regulation via hormonal, metabolic, and immune rhythms. The relevant claim is: malignancy is associated with degradation of *multi-source temporal coordination*, including but not limited to neural, endocrine, and local tissue clocks.

7.3 Perineural Invasion Reinterpreted

The known clinical phenomenon of tumors growing along nerves (perineural invasion) [18, 19] is typically interpreted as mechanical spread. Our framework suggests an additional interpretation: cancer cells may be hijacking high-bandwidth signaling channels for growth support, exploiting the physical coupling substrate while remaining relatively insensitive to termination control. The tumor microenvironment recruits neural tissue; autonomic nerves innervate tumors and provide neurotransmitters (norepinephrine, acetylcholine) that alter the tumor microenvironment [18]. The brain can also supply doublecortin-expressing neural progenitor cells to developing tumors via the bloodstream [19], suggesting brain-tumor communication (“tumorception”). Neural coupling is therefore one high-bandwidth example, not a required substrate of malignancy: the boundary-failure claim is informational and applies equally to non-neural coupling channels (paracrine, mechanical, immune, and junctional).

8 Immune Evasion as Loss of Distinguishability

The immune system is the organism’s primary boundary-enforcement mechanism. Its logic resembles a decision function that maps high-dimensional cellular states into discrete actions (kill/ignore). This requires *distinguishable inputs*; cells must present features detectably different from self. In practice this decision is criterion-based, not binary: tumors can remain partly distinguishable while net signal quality is too low for reliable action. Formally, if Z denotes the immune-visible feature set (antigen presentation, checkpoint context, inflammatory state) and $D \in \{\text{clear, tolerate}\}$ the effective immune decision, then reliability depends on positive decision information $I(Z; D)$. Evasion programs do not need to eliminate all signal; they need only reduce actionable information enough to drive decision quality toward chance.

8.1 The PD-1/PD-L1 Checkpoint Axis

Cancer exploits the PD-1/PD-L1 checkpoint axis [27] to reduce immune visibility. PD-1 is a checkpoint receptor on T cells that limits excessive stimulation. Tumor PD-L1 engages PD-1 and suppresses T-cell activation, enabling immune escape. This is a boundary failure at the immune interface: tumor cells use a normal self-protection pathway to avoid elimination.

Checkpoint inhibitor therapy (anti-PD-1/PD-L1 antibodies) works by *restoring distinguishability*: blocking the false “self” signal so that the immune system can detect and

eliminate cancer cells [28]. In our framework, this corresponds to “forced distinction”, the therapeutic principle derived from the boundary logic failure model.

8.2 Secondary Boundary Failures

Some cancers develop resistance to checkpoint blockade through secondary boundary failures [28]: JAK1/JAK2 mutations that impair interferon- γ responsiveness (blocking the information channel that normally induces PD-L1 expression), loss of β 2-microglobulin eliminating MHC class I surface expression (removing the very molecules through which cells present antigens to T cells), and PTEN loss decreasing T cell infiltration. Each represents a further layer of boundary dissolution.

8.3 Gap Junctions and Antigen Broadcast

Immune evasion is often framed as a surface receptor problem (PD-L1). An additional mechanism is the failure of *broadcast*. Gap junctions have been shown to transfer antigenic peptides directly to dendritic cells for cross-presentation [37]. Connexin downregulation in cancer therefore also represents decoupling from the tissue’s immune surveillance network, reducing the cell’s informational visibility to organism-level control.

9 Thermodynamic Perspective: Cost Externalization

9.1 The Warburg Effect as Metabolic Decoupling

Cancer cells often shift toward aerobic glycolysis (Warburg effect [29]). This mode is less ATP-efficient but supports rapid biomass accumulation [30, 31]. In this framework, the shift is not attributed only to mitochondrial dysfunction; it is also a marker of reduced coupling to organism-level metabolic coordination.

Normal oxidative phosphorylation depends on coordinated oxygen delivery, circadian metabolic timing, and tissue nutrient allocation. Aerobic glycolysis is more autonomous and can proceed with weaker systemic coordination. The cancer cell trades efficiency for autonomy, aligning with atavistic predictions of reversion to older metabolic programs [4].

The Warburg shift can also be read as a mechanism to support high-entropy proliferative states without sacrificing regulatory order. Maintaining a low-entropy differentiated state requires continuous ATP to suppress transcriptional noise [38]. Malignancy expands the metabolic budget to support both proliferation and active evasion (Active Masking), increasing organism-level burden.

9.2 Cachexia as Systemic Cost Payment

Cancer-associated cachexia (involuntary weight loss, muscle wasting, and metabolic disruption) affects 50–85% of cancer patients and contributes to 20% of cancer deaths [32, 33]. It cannot be reversed by nutritional supplementation alone, distinguishing it from simple malnutrition.

In our framework, cachexia reflects interacting mechanisms rather than a single “cost transfer” process: (i) direct substrate burden from tumor glucose/amino-acid demand, (ii) metabolic expansion to sustain high-coherence proliferation (budget escape), and (iii) inflammatory catabolism driven by tumor-immune interaction. The host’s attempts to meet tumor demand via muscle proteolysis and adipose lipolysis generate the cachexia phenotype, while cytokine signaling (IL-6, TNF- α , TGF- β) amplifies tissue wasting [32]. Host catabolic breakdown products are in turn available as substrates for further tumor proliferation, creating a positive feedback loop between tumor growth and systemic wasting.

This is not a violation of thermodynamics. It is a redistribution across scales: local proliferative advantage with expanded metabolic capacity is coupled to global host burden and inflammatory wasting.

9.3 Entropy Production (Heuristic)

We use entropy-production language as an organizing heuristic, not as a first-principles law for all tumors. A conservative statement is that thermodynamic load tracks proliferative burden:

$$\dot{S}_{\text{tumor}}(t) \propto N_{\text{tumor}}(t), \quad (10)$$

where $N_{\text{tumor}}(t)$ is an effective tumor burden proxy. If tumor burden grows approximately as $N_{\text{tumor}}(t) \sim e^{rt}$ over a phase of progression, then the associated thermodynamic load can also rise approximately exponentially over that phase.

In this framing, disease progression reaches a *critical transition* when tumor-driven load exceeds host dissipation and repair capacity. The term “event horizon” is metaphorical shorthand for that qualitative threshold, not a literal physical singularity.

10 Toy Formalism: Tissue as a Labeled Graph

10.1 State Variables

We model a tissue region as a labeled graph $\mathcal{T} = (V, E)$, where each node $i \in V$ is a cell and each edge $(i, j, \ell) \in E$ carries a label ℓ indicating the type of coupling.

Each cell carries:

- a discrete state $x_i \in \{\text{Healthy}, \text{PreCancer}, \text{Cancer}\}$,
- an identity-alignment scalar $p_i \in [0, 1]$ (interpretable as “organism alignment”),
- an energetic cost proxy $\epsilon_i > 0$, and
- a division-rate proxy $r_i \geq 0$.

Edges include (at minimum):

- *Regulatory/signaling* (SIG): growth inhibition, differentiation cues, contact inhibition
- *Lineage* (DIV): division history (parent-child)

- *Temporal coordination* (TMP): shared timing fields (circadian, hormonal)
- *Harmonic/adhesion* (HAR): tissue adhesion, gap junction communication

10.2 A Coherence Metric

We define a scalar coherence score $\kappa \in [0, 1]$ intended to summarize: (i) density of regulatory signaling, (ii) temporal alignment, and (iii) identity commitment (low entropy).

Let ρ_{sig} be the fraction of regulatory edges among all edges, and let ρ_{tmp} be an analogous proxy for temporal coordination. Let H be the mean Shannon entropy of the binary distribution $(p_i, 1 - p_i)$ for each cell's alignment scalar $p_i \in [0, 1]$ (1.0 for fully organism-aligned, 0.0 for fully self-aligned). This is a proxy for identity ambiguity/commitment: H is maximal near $p_i = 0.5$ and minimal near $p_i \in \{0, 1\}$. It does *not* measure spatial heterogeneity across cells; it measures per-cell identity ambiguity.

$$H = \frac{1}{|V|} \sum_{i \in V} [-p_i \log_2 p_i - (1 - p_i) \log_2(1 - p_i)] \quad (11)$$

We then combine these terms in a simple convex score:

$$\kappa = \text{clip}_{[0,1]}(a\rho_{\text{sig}} + b\rho_{\text{tmp}} + c(1 - H)) \quad (12)$$

with weights $a, b, c \geq 0$ and $a + b + c = 1$. This definition provides a quantitative (albeit simplified) metric for tissue health, ranging from $\kappa \approx 1$ (perfectly healthy) to $\kappa \approx 0$ (terminal/metastatic).

Coherence (κ)	Interpretation
0.9 – 1.0	Healthy tissue
0.7 – 0.9	Normal tissue with minor perturbation
0.5 – 0.7	Pre-cancerous state
0.3 – 0.5	Early malignancy
0.1 – 0.3	Advanced malignancy
0.0 – 0.1	Terminal/Metastatic

Table 3: Coherence interpretation. These ranges are illustrative, not clinically calibrated.

10.3 Cancer Transform Operator

We define a cancer transform operator C that acts on a node and its incident relations:

- Alignment collapse: $p_i \rightarrow 0.05$ (self-dominant control)
- Coupling weakening: progressively reduce HAR coupling as cancer lineages expand with weak adhesion reconnection
- Edge pruning: remove SIG/TMP edges; retain DIV lineage edges
- Energy draw: $\epsilon_i \rightarrow \gamma \epsilon_i$ with $\gamma > 1$ (Warburg-proxy burden)
- Recursion: add copy(node) via a DIV edge (the `rec_succ` step)

11 Toward Measurable Proxies

For this framework to move beyond a conceptual model, the abstract variables must map to measurable quantities. We propose the following candidate proxies:

Abstract Variable	Candidate Proxy	Measurement Method
Identity alignment (p_i)	Differentiation state / marker expression	Flow cytometry, immunohistochemistry
Signaling density (ρ_{sig})	Gap junction communication	Connexin expression [34], FRAP assays
Temporal coordination (ρ_{tmp})	Circadian gene coherence	Bmal1/Clock/Per expression across tissue (qPCR, scRNA-seq) [23]
Identity entropy (H)	Transcriptional Entropy (SCENT/mRNAsi)	Signaling Entropy [39], Stemness Index [40]
Coherence (κ)	Composite tissue coordination	Combination of above metrics
Bioelectric coupling	Membrane voltage gradients	Voltage-sensitive fluorescent dyes [17]

Table 4: Candidate measurable proxies for abstract framework variables.

The theoretical variable H (identity entropy) can be operationalized with Signaling Entropy (SCENT), which quantifies promiscuity in the protein interaction network. High entropy correlates with stem-like undifferentiated states and poorer prognosis, supporting the prediction that malignancy is a high-entropy, low-constraint state.

Loss of gap junction-mediated intercellular communication (GJIC) is associated with malignancy across multiple cancer types. Reduced connexin expression correlates with functional communication loss [34]. Transgenic mice lacking Cx32 or Cx43 show higher tumorigenesis risk [34]. This provides a measurable correlate for “signaling density.”

Levin’s work also shows that membrane voltage can be both a detection modality for tumors (distinct electrical impedance) and a functional regulator of oncogene-driven tumorigenesis [17]. This supports “bioelectric coupling” as a measurable axis. Direct causal links from voltage perturbation to antigen-presentation phenotypes (for example, MHC-I modulation) remain downstream hypotheses that require targeted tests.

12 Therapeutic Design Principle: Restore Observability and Enforce Termination

In the boundary-failure framing, therapies succeed when they restore boundary observability between malignant cells and organism-level control systems. We propose this as a unifying design principle, not as a claim about any single regimen.

12.1 Force Distinction

Increase discriminability of malignant cells relative to self:

- **Neoantigen presentation:** Personalized cancer vaccines that force expression of tumor-specific antigens.
- **Checkpoint inhibition:** Anti-PD-1/PD-L1 antibodies that remove the false “self” signal, restoring immune visibility [27].
- **Differentiation therapy:** A key example is all-trans retinoic acid (ATRA) in acute promyelocytic leukemia (APL). ATRA drives leukemic blasts into mature granulocytes, with complete remission rates above 90% [25, 26], *without direct cytotoxic killing*. In this framework, the intervention restores boundary observability by forcing stable differentiated identity.
- **Bispecific antibodies / CAR-T:** Engineered molecular bridges that force immune cell engagement with cancer cells, creating the distinction that cancer had dissolved.

12.2 Restore Termination Predicates

Re-enable growth arrest, senescence, or apoptosis pathways:

- p53 reactivation [13]
- Synthetic “stop” signals
- CDK inhibitors that enforce cell cycle checkpoints

12.3 Re-couple to Tissue Constraints

Reconstruct regulatory edges that impose contact inhibition and signaling coherence:

- Bioelectric reprogramming: manipulation of ion channels and gap junctions to restore collective voltage patterns that suppress tumorigenesis [16, 17]
- Chronotherapy: restoration of circadian regulation via clock-derived nanovesicles or timed drug administration [23]

12.4 Constrain Resource Externalization

Reduce the ability to offload metabolic and inflammatory costs onto the host:

- Metabolic inhibitors (e.g., 2-deoxyglucose, metformin) that increase the energetic cost of the Warburg phenotype
- Anti-cachexia interventions that protect host tissue from tumor-driven catabolism [32]

13 Clinical Correlations and Testable Hypotheses

The framework suggests qualitative hypotheses that can be checked against known clinical patterns and tested prospectively.

1. **Immune observability has multiple failure modes:** Boundary loss can appear either as *active masking* (immune-visible but vetoed) or *decoherence/invisibility* (reduced effective distinguishability). *Testable:* PD-L1/MHC-I status should partition tumors into at least two modes with distinct coherence-proxy profiles: a checkpoint-engaged, clock-structured mode and a low-observability mode with weaker antigen-presentation features.
2. **Cachexia as cost externalization:** Systemic wasting can be interpreted as host-level payment for proliferative burden. *Testable:* Tumor metabolic rate (FDG-PET) should correlate with cachexia severity after controlling for tumor mass.
3. **Circadian disruption precedes malignancy:** Circadian disruption should raise boundary-failure probability by degrading checkpoint timing coordination. *Testable:* Circadian structure in peri-tumoral tissue should deviate from matched normal tissue *before* overt malignancy is detectable (for example, increased dispersion or pathologic locking signatures). IARC night-shift data already provides population-level support [20, 21].
4. **Spontaneous remission as re-entanglement:** Rare immune-mediated regressions can be viewed as abrupt restoration of observability. *Testable:* Documented spontaneous remission cases [35] should show measurable immune reactivation (increased CD8+ T cell infiltration, pro-inflammatory cytokine surge) preceding tumor regression, with concurrent acute infections providing the immune trigger [36].
5. **Perineural invasion correlates with boundary loss:** Tumors with greater perineural invasion [18] should show lower coherence-proxy metrics and worse prognosis; in immunotherapy-treated cohorts, it may associate with reduced checkpoint-blockade response (since neural hijacking indicates deeper boundary failure).
6. **Bioelectric disconnection as early marker:** Changes in membrane voltage patterns should precede overt malignancy and predict tumor formation [17]. Levin's tadpole experiments demonstrate this in principle: voltage management prevents tumor formation despite active oncogene expression.
7. **Growth-stability falsifier:** Any lineage showing persistently elevated proliferative throughput and high coherence without corresponding increase in control investment would challenge the control-budget formulation (Equation 8). *Update:* TCGA analysis reveals positive correlation between proliferation and coherence markers in many cohorts, supporting a "budget escape" model where tumors expand metabolic capacity rather than trading off fixed resources.

14 Empirical Validation: TCGA Cohort Analysis

To ground the framework’s predictions in existing data, we ran correlation, subtype, and survival analyses using bulk RNA-seq expression from The Cancer Genome Atlas (TCGA), accessed through the ISB Cancer Genomics Cloud BigQuery tables [44]. We analyzed six cohorts spanning $n = 3,611$ tumor samples: TCGA-SKCM (melanoma, $n = 472$), TCGA-LUAD (lung adenocarcinoma, $n = 530$), TCGA-BRCA (breast, $n = 1,113$), TCGA-COAD (colon, $n = 473$), TCGA-HNSC (head and neck squamous cell carcinoma, $n = 522$), and TCGA-LUSC (lung squamous cell carcinoma, $n = 501$). We extracted transcripts-per-million (TPM) values for 21 target genes spanning immune checkpoint (CD274/PD-L1, PDCD1LG2, PDCD1), MHC class I (HLA-A, HLA-B, HLA-C, B2M), gap junction (GJA1/Cx43, GJB2/Cx26, GJA5/Cx40, GJB6/Cx30), circadian clock (ARNTL/BMAL1, CLOCK, PER1, PER2, CRY1, CRY2), and differentiation markers (CDH1, VIM, MYC, TP53). Correlations were computed at tumor-sample level (Spearman ρ on $\log_2(\text{TPM}+1)$, with FDR correction). Survival was analyzed at patient level after retaining one tumor sample per case before clinical merge ($n = 3,089$ valid OS cases). We report both raw log-rank p values and Benjamini–Hochberg adjusted q values. For SKCM and LUAD robustness checks, we fit multivariable Cox models with clinical covariates (age, sex, and stage as categorical indicators), tested a continuous PD-L1 \times clock interaction term, and applied BH correction across pre-specified primary robustness tests.

Notation: unless explicitly stated otherwise, asterisks in TCGA result figures indicate FDR-significant results ($q < 0.05$) after the correction scope used for that analysis.

Evidence reporting convention: to avoid over- or under-stating results, we label each endpoint as *FDR-significant* ($q < 0.05$), *nominal/directional* (raw $p < 0.05$ but $q \geq 0.05$), or *non-significant*. Nominal and non-significant findings are retained for transparency and hypothesis generation, but are not interpreted as confirmatory evidence.

For auditability, Table 5 reports all pre-specified inferential endpoints in this manuscript (survival, primary robustness, and circadian stage tests) with raw p , corrected q , and category labels. Across these 32 endpoints, 4 are FDR-significant, 3 are nominal, and 25 are non-significant.

14.1 Circadian Coherence and PD-L1

We defined a per-sample circadian coherence proxy as the coefficient of variation (CV) across the six core clock genes (ARNTL, CLOCK, PER1, PER2, CRY1, CRY2), where lower CV indicates more uniform (coherent) clock-gene expression. Because this is a within-sample cross-gene dispersion metric from bulk RNA-seq, it is interpreted as a transcriptional clock-structure proxy rather than a direct estimate of circadian phase coherence over time. The initial Hypothesis 1 expectation was that checkpoint engagement would track reduced coherence; the TCGA data instead support a refined two-mode structure in which checkpoint-high tumors can show clock restructuring/locking (Active Masking) rather than simple temporal decoherence.

The circadian CV showed a significant negative correlation with PD-L1 expression in **all six cohorts** (100% replication rate, all FDR $q < 0.05$):

- TCGA-SKCM: $\rho = -0.381$, $p = 9.6 \times 10^{-18}$, $n = 472$

Table 5: Pre-specified endpoint evidence table (audit view). This table lists all pre-specified endpoint families used for inferential claims in this manuscript: 12 survival tests (BH across all survival tests), 8 primary robustness Cox tests (BH across primary robustness tests), and 12 circadian stage tests (q-values from global BH correction in `master_fdr_results.csv`). Categories: FDR-significant ($q < 0.05$), Nominal ($p < 0.05$ with $q \geq 0.05$), and Non-significant.

Family	Cohort	Endpoint	p	q	Category
Survival	BRCA	AM vs DC	0.5084	0.7627	Non-significant
Survival	BRCA	Q1 vs Q4	0.3822	0.7414	Non-significant
Survival	COAD	AM vs DC	0.3050	0.7319	Non-significant
Survival	COAD	Q1 vs Q4	0.7102	0.8397	Non-significant
Survival	HNSC	AM vs DC	0.1283	0.5133	Non-significant
Survival	HNSC	Q1 vs Q4	0.7599	0.8397	Non-significant
Survival	LUAD	AM vs DC	0.0489	0.2937	Nominal
Survival	LUAD	Q1 vs Q4	0.7698	0.8397	Non-significant
Survival	LUSC	AM vs DC	0.8641	0.8641	Non-significant
Survival	LUSC	Q1 vs Q4	0.4325	0.7414	Non-significant
Survival	SKCM	AM vs DC	0.0011	0.0132	FDR-significant
Survival	SKCM	Q1 vs Q4	0.2545	0.7319	Non-significant
Robustness	LUAD	AM vs DC (adjusted)	0.0114	0.0454	FDR-significant
Robustness	LUAD	AM vs DC + PD-L1/B2M	0.0343	0.0686	Nominal
Robustness	LUAD	Clock effect (high PD-L1)	0.0785	0.1257	Non-significant
Robustness	LUAD	PD-L1 \times Clock interaction	0.2401	0.2744	Non-significant
Robustness	SKCM	AM vs DC (adjusted)	0.0286	0.0686	Nominal
Robustness	SKCM	AM vs DC + PD-L1/B2M	0.1305	0.1740	Non-significant
Robustness	SKCM	Clock effect (high PD-L1)	0.2760	0.2760	Non-significant
Robustness	SKCM	PD-L1 \times Clock interaction	0.0075	0.0454	FDR-significant
Stage (Circadian)	BRCA	Kruskal-Wallis	0.4622	0.5475	Non-significant
Stage (Circadian)	BRCA	Spearman trend	0.2685	0.3485	Non-significant
Stage (Circadian)	COAD	Kruskal-Wallis	0.2433	0.3227	Non-significant
Stage (Circadian)	COAD	Spearman trend	0.4346	0.5224	Non-significant
Stage (Circadian)	HNSC	Kruskal-Wallis	0.0512	0.0827	Non-significant
Stage (Circadian)	HNSC	Spearman trend	0.0287	0.0500	FDR-significant
Stage (Circadian)	LUAD	Kruskal-Wallis	0.9753	0.9793	Non-significant
Stage (Circadian)	LUAD	Spearman trend	0.8202	0.8664	Non-significant
Stage (Circadian)	LUSC	Kruskal-Wallis	0.5497	0.6267	Non-significant
Stage (Circadian)	LUSC	Spearman trend	0.8428	0.8864	Non-significant
Stage (Circadian)	SKCM	Kruskal-Wallis	0.7567	0.8204	Non-significant
Stage (Circadian)	SKCM	Spearman trend	0.4718	0.5535	Non-significant

- TCGA-LUAD: $\rho = -0.303$, $p = 1.1 \times 10^{-12}$, $n = 530$
- TCGA-BRCA: $\rho = -0.222$, $n = 1,113$
- TCGA-COAD: $\rho = -0.312$, $n = 473$
- TCGA-HNSC: $\rho = -0.125$, $n = 522$
- TCGA-LUSC: $\rho = -0.142$, $n = 501$

Higher PD-L1 expression tracks *lower* circadian CV (more coherent clock expression) across all six cancer types. At first glance, this conflicts with a simple degraded-coordination expectation for checkpoint-engaged tumors. A plausible interpretation is an *immune-hot* state: interferon- γ signaling from infiltrating T cells can co-activate PD-L1 and other immune-responsive transcriptional programs [27, 28], producing an inflamed but checkpoint-protected microenvironment. In this setting, boundary failure is *active masking* rather than temporal decoherence alone; PD-L1 upregulation acts as adaptive evasion in tumors that still respond to immune pressure. Because these data are bulk RNA-seq, the mechanism is interpretive rather than causal proof. In sensitivity analyses controlling for purity and microenvironment covariates, the circadian CV–PD-L1 association remained negative in both discovery cohorts (SKCM partial $r = -0.238$, $p = 4.29 \times 10^{-5}$; LUAD partial $r = -0.144$, $p = 0.00658$; Section 14.8). Replication across six tissue contexts supports generalizability of direction, while effect magnitude is heterogeneous (for example, weaker in HNSC/LUSC than in SKCM/LUAD).

Among individual clock genes, ARNTL (BMAL1) showed the strongest positive association with PD-L1 (SKCM: $\rho = +0.428$, $p = 1.9 \times 10^{-22}$; LUAD: $\rho = +0.287$, $p = 1.6 \times 10^{-11}$), while PER1 was negatively correlated in both cohorts (SKCM: $\rho = -0.136$, $p = 0.003$; LUAD: $\rho = -0.099$, $p = 0.023$). The divergent directions within the clock network, BMAL1/CLOCK positively associated and PER genes negatively associated, suggest that PD-L1-high tumors exhibit *restructured* rather than uniformly disrupted circadian programs. Figure 4 summarizes the cross-cancer correlation structure.

14.2 PD-L1 and MHC Class I Co-regulation

PD-L1 expression was strongly positively correlated with MHC class I components in both cohorts:

- B2M: SKCM $\rho = +0.760$ ($p = 7.0 \times 10^{-90}$); LUAD $\rho = +0.555$ ($p = 3.7 \times 10^{-44}$)
- HLA-B: SKCM $\rho = +0.717$ ($p = 1.3 \times 10^{-75}$); LUAD $\rho = +0.547$ ($p = 1.2 \times 10^{-42}$)

This co-upregulation is consistent with shared IFN- γ transcriptional regulation, as both PD-L1 and MHC-I are interferon-responsive [27, 28]. In the boundary framework, this identifies a specific failure mode: the antigen-presentation channel (MHC-I) is intact, but the organism’s clearance decision is overridden by checkpoint engagement (PD-L1). The boundary remains visible, but the response is *vetoed*. This refines Hypothesis 1: the most clinically relevant boundary failure is not always loss of distinguishability *per se*, but suppression of the organism’s *response* to detected distinction.

14.3 Gap Junction Expression

Connexin transcript levels showed weak positive correlations with PD-L1 (GJA1/Cx43: SKCM $\rho = +0.105$, $p = 0.023$; LUAD $\rho = +0.125$, $p = 0.004$), rather than the predicted inverse relationship. Gap junction composite expression was uncorrelated with MHC-I composite in SKCM ($\rho = +0.006$, $p = 0.89$) and weakly positive in LUAD ($\rho = +0.155$, $p = 0.0003$).

This is consistent with a known limitation of bulk RNA-seq: connexin transcript levels do not capture functional gap-junction intercellular communication (GJIC), which depends on protein localization, phosphorylation state, and channel gating [34]. Many connexins are post-translationally regulated, and some (e.g., Cx43) are internalized or phosphorylated to close channels without transcript-level changes. Given small effect sizes and proxy mismatch, these transcript-level gap-junction associations are treated as non-confirmatory. Testing the gap-junction arm of Hypothesis 1 requires functional assays (FRAP, scrape-loading, or dye transfer) rather than expression-level proxies.

14.4 Summary of Key Correlations

The circadian–checkpoint coupling replicates across all six cancer types. Table 6 summarizes the primary Spearman correlations for the two discovery cohorts; Figure 4 presents the full cross-cancer correlation heatmap.

Comparison	Category	TCGA-SKCM		TCGA-LUAD	
		ρ	p	ρ	p
CD274 vs Circadian CV	Coherence	-0.381	9.6×10^{-18}	-0.303	1.1×10^{-12}
CD274 vs ARNTL	Clock	+0.428	1.9×10^{-22}	+0.287	1.6×10^{-11}
CD274 vs PER1	Clock	-0.136	3.1×10^{-3}	-0.099	2.3×10^{-2}
CD274 vs B2M	MHC-I	+0.760	7.0×10^{-90}	+0.555	3.7×10^{-44}
CD274 vs GJA1	Gap jcn.	+0.105	2.3×10^{-2}	+0.125	3.9×10^{-3}
GJ mean vs MHC-I mean	Cross	+0.006	0.89	+0.155	3.3×10^{-4}
CDH1 vs VIM	EMT	-0.132	4.1×10^{-3}	+0.110	1.2×10^{-2}

Table 6: Spearman correlations for Hypothesis 1 target genes in TCGA tumor samples (discovery cohorts). Data source: ISB-CGC BigQuery ([\(isb-cgc-bq.TCGA.RNAseq_hg38_gdc_r35\)](#); see extraction manifest for exact table IDs). All values are $\log_2(\text{TPM}+1)$ -transformed. Cross-cancer replication is shown in Figure 4. Extraction and analysis scripts are available in the companion repository under `experiments/tcga/`.

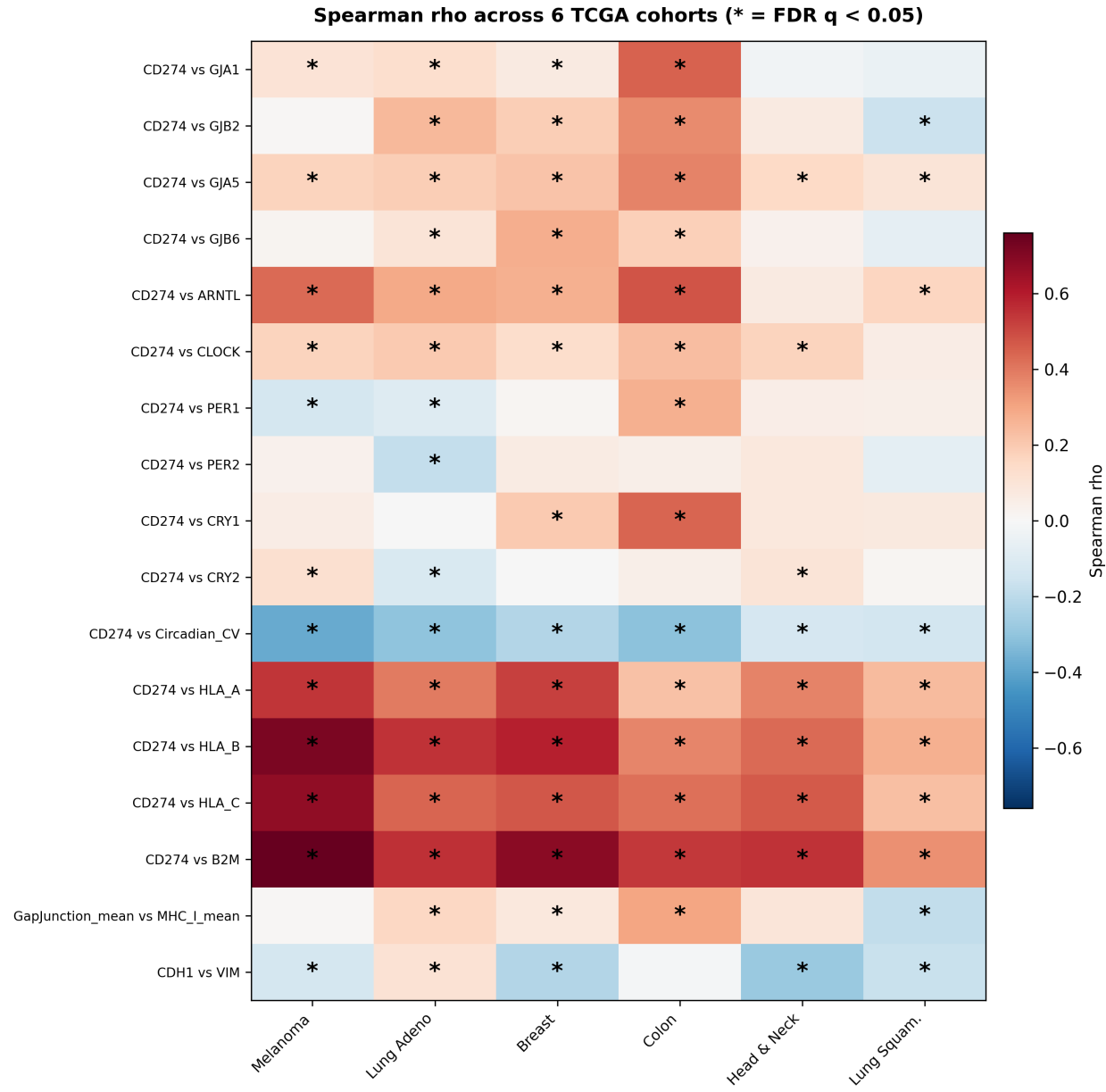


Figure 4: Cross-cancer correlation heatmap for key framework predictions across all six TCGA cohorts ($n = 3,611$ tumors). The circadian CV vs. PD-L1 negative correlation (top row) replicates in all six cancer types (100% replication rate). Color intensity reflects Spearman ρ ; asterisks denote FDR-corrected significance.

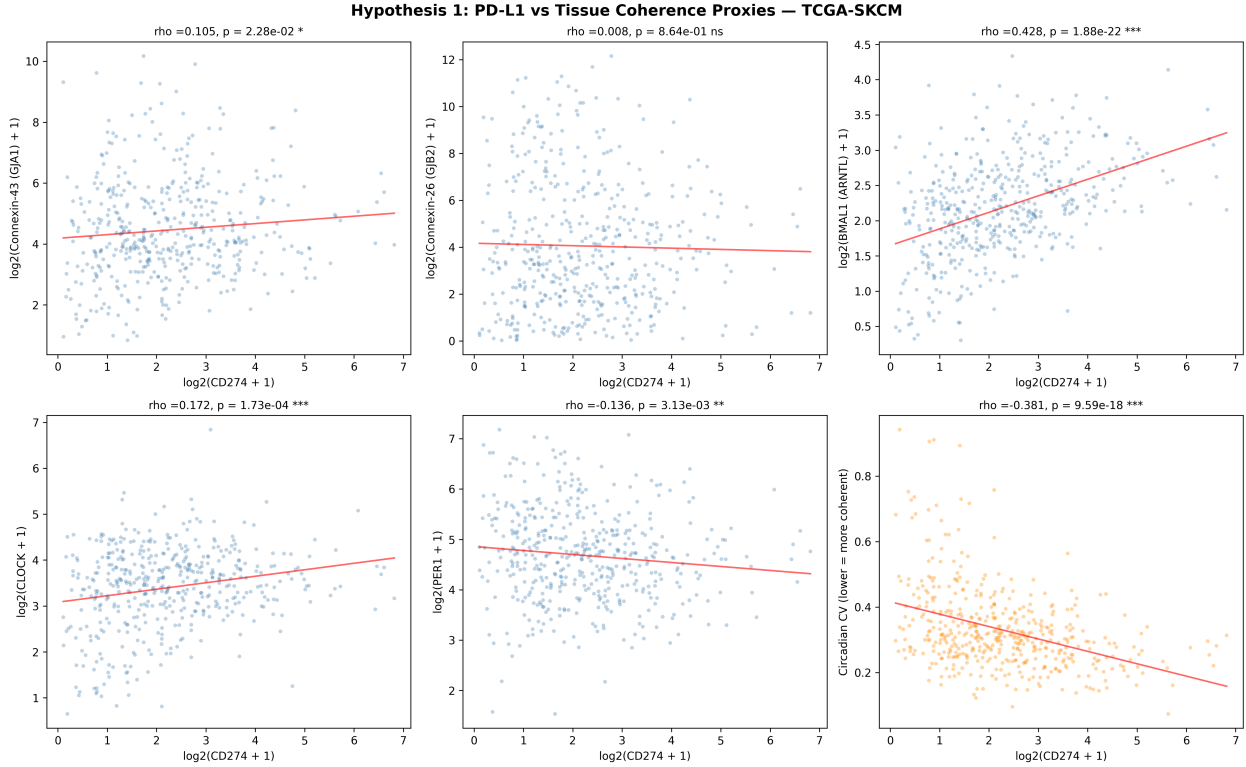


Figure 5: Hypothesis 1 validation in TCGA-SKCM (melanoma, $n = 472$ tumor samples). PD-L1 (CD274) expression vs. gap junction genes (GJA1, GJB2), clock genes (ARNTL, CLOCK, PER1), and circadian coherence (CV). The circadian CV panel (bottom right, orange) shows the strongest signal: higher PD-L1 correlates with lower CV (more coherent clock expression), consistent with the immune-hot phenotype.

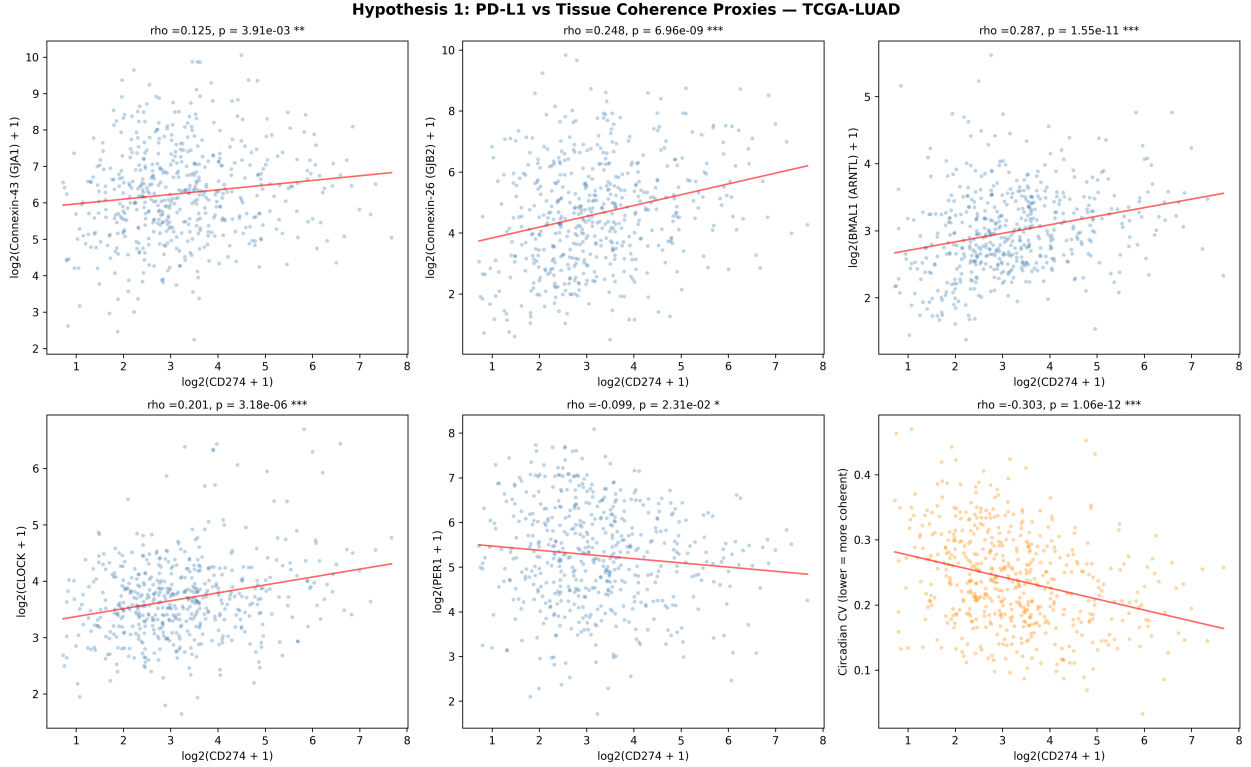


Figure 6: Hypothesis 1 validation in TCGA-LUAD (lung adenocarcinoma, $n = 530$ tumor samples). The same pattern replicates across a second cancer type, supporting the generalizability of the circadian–checkpoint coupling.

14.5 Tumor vs. Matched Normal Tissue

A critical test of the boundary-failure framework is whether tumor circadian programs differ systematically from matched normal tissue. If cancer simply “breaks” the clock, tumors should show higher circadian CV (more disordered clock expression) than matched normals. We compared circadian CV between tumor and matched normal samples in five cancer types with sufficient normal tissue representation (SKCM was excluded due to limited normal samples).

Contrary to the naive “broken clock” prediction, tumors showed **lower** circadian CV than matched normals in four of five cancer types tested:

- TCGA-LUAD: $p = 2.28 \times 10^{-6}$
- TCGA-BRCA: $p = 5.13 \times 10^{-9}$
- TCGA-HNSC: $p = 7.0 \times 10^{-7}$
- TCGA-LUSC: $p = 8.6 \times 10^{-7}$
- TCGA-COAD: not significant

Tumors show *lower* circadian CV (more uniform clock-gene expression) than matched normal tissue, not higher. This supports a “locked, not broken” *transcriptional* restructuring interpretation: the clock-gene program appears co-opted rather than simply disrupted. Because CV is a within-sample cross-gene dispersion proxy from bulk RNA-seq, it does not establish temporal phase coherence or rhythmicity; time-series and single-cell assays are required for that. Figures 7 and 8 show paired comparisons and cohort-level summary statistics.

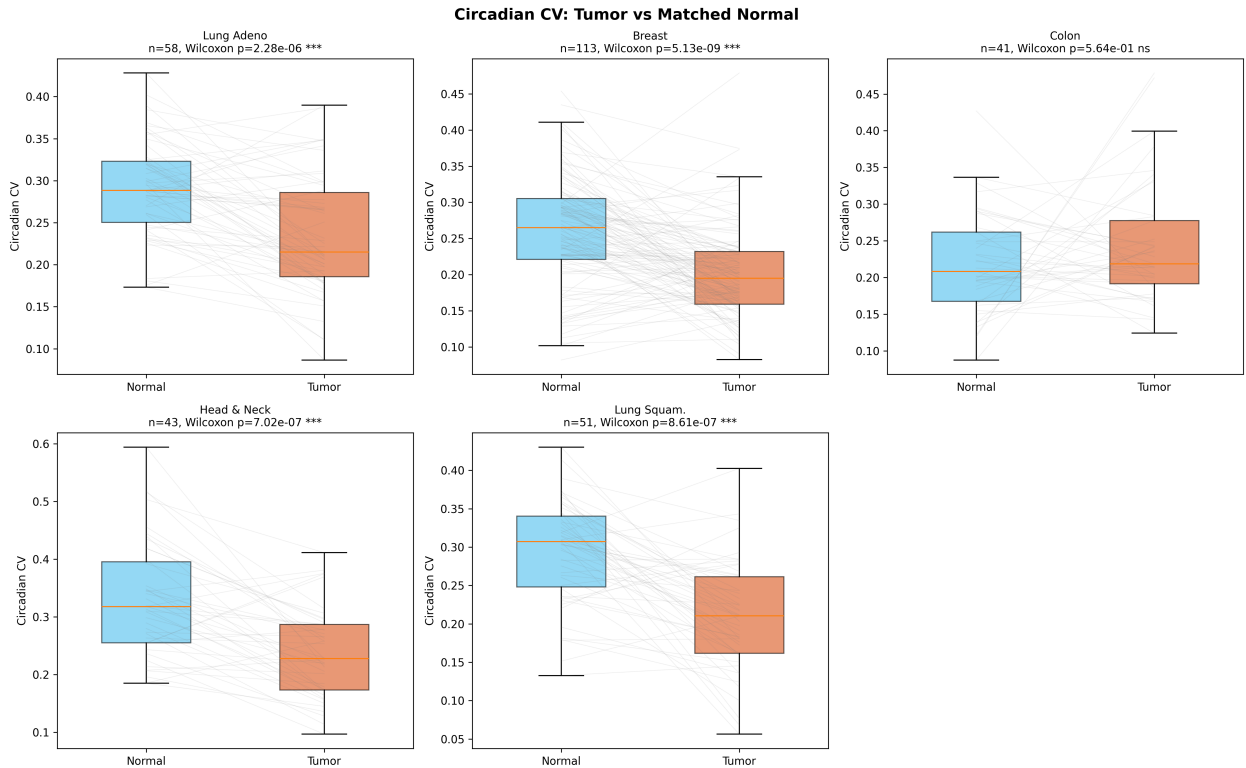


Figure 7: Circadian CV in tumor vs. matched normal tissue across five TCGA cancer types. Tumors show significantly *lower* CV (more uniform clock-gene expression) than matched normals in 4/5 cancer types, supporting a transcript-level “locked, not broken” restructuring signature in this proxy.

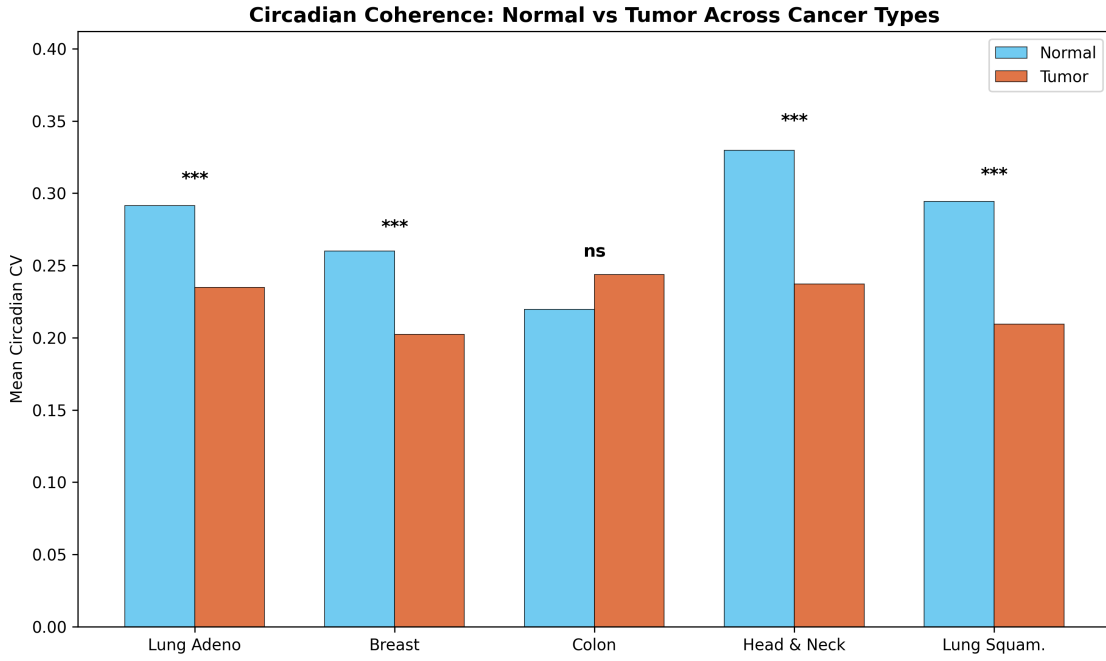


Figure 8: Cohort-level summary of tumor-minus-normal circadian CV shifts across five TCGA cancer types. Four cohorts show negative deltas (tumor lower than normal), while COAD is near-neutral/non-significant, matching the paired-sample analysis.

14.6 Active Masking vs. Temporal Decoherence Classification

The circadian–checkpoint coupling and tumor–normal comparisons suggest that boundary failure in cancer is not monolithic. To formalize this, we classified tumors into boundary-failure subtypes based on expression of key framework genes:

- **Active Masking:** high PD-L1 (CD274) + high BMAL1 (ARNTL) + low PER1. These tumors retain a functional but restructured clock and deploy checkpoint molecules to veto immune clearance. The boundary is visible but *vetoed*.
- **Temporal Decoherence:** low PD-L1 + low B2M. These tumors have lost both checkpoint engagement and antigen-presentation capacity. The boundary is *invisible*.
- **Mixed:** all remaining tumors not classified into either category.

Thresholds were set at median expression within each cancer type. Active Masking tumors showed significantly **lower** circadian CV than Decoherence tumors in **all six cancer types** (Kruskal–Wallis FDR $q < 10^{-9}$; pairwise AM-vs-DC Mann–Whitney FDR $q < 10^{-4}$). This is consistent with the two boundary-failure modes having distinct circadian architectures: Active Masking tumors maintain tight clock coordination, while Decoherence tumors show variable and disordered circadian programs. Figure 9 shows that both modes are represented in every cohort, and Figure 11 shows their separation in checkpoint-clock expression space. Because subtype definitions include ARNTL and PER1, the CV contrast is interpreted as internal-consistency evidence rather than an independent validation endpoint.

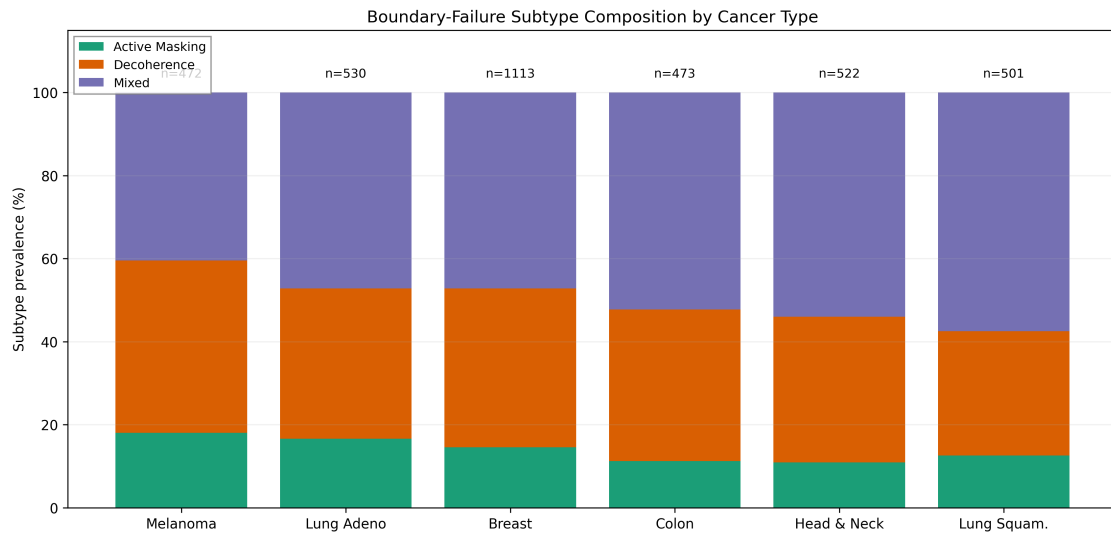


Figure 9: Boundary-failure subtype composition across six TCGA cohorts. Active Masking, Decoherence, and Mixed classes are all present in each cohort, supporting a multi-mode rather than single-mode failure landscape.

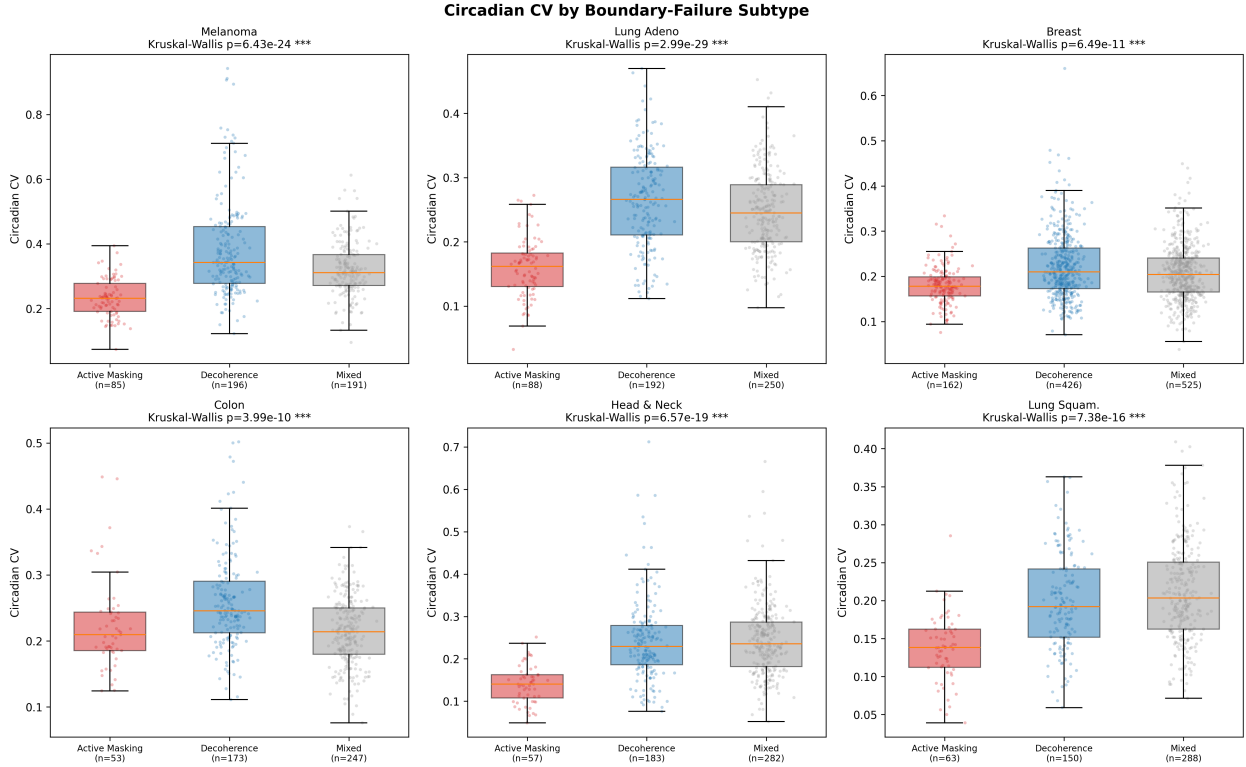


Figure 10: Circadian CV by boundary-failure subtype across six TCGA cancer types. Active Masking tumors (high PD-L1, high BMAL1, low PER1) show consistently lower CV than Decoherence tumors (low PD-L1, low B2M) in all six cancer types (Kruskal–Wallis FDR $q < 10^{-9}$; pairwise AM-vs-DC Mann–Whitney FDR $q < 10^{-4}$), consistent with distinct circadian architectures for different boundary-failure modes. Because subtype definitions include ARNTL/PER1, this is interpreted as internal-consistency evidence rather than an independent validation endpoint.

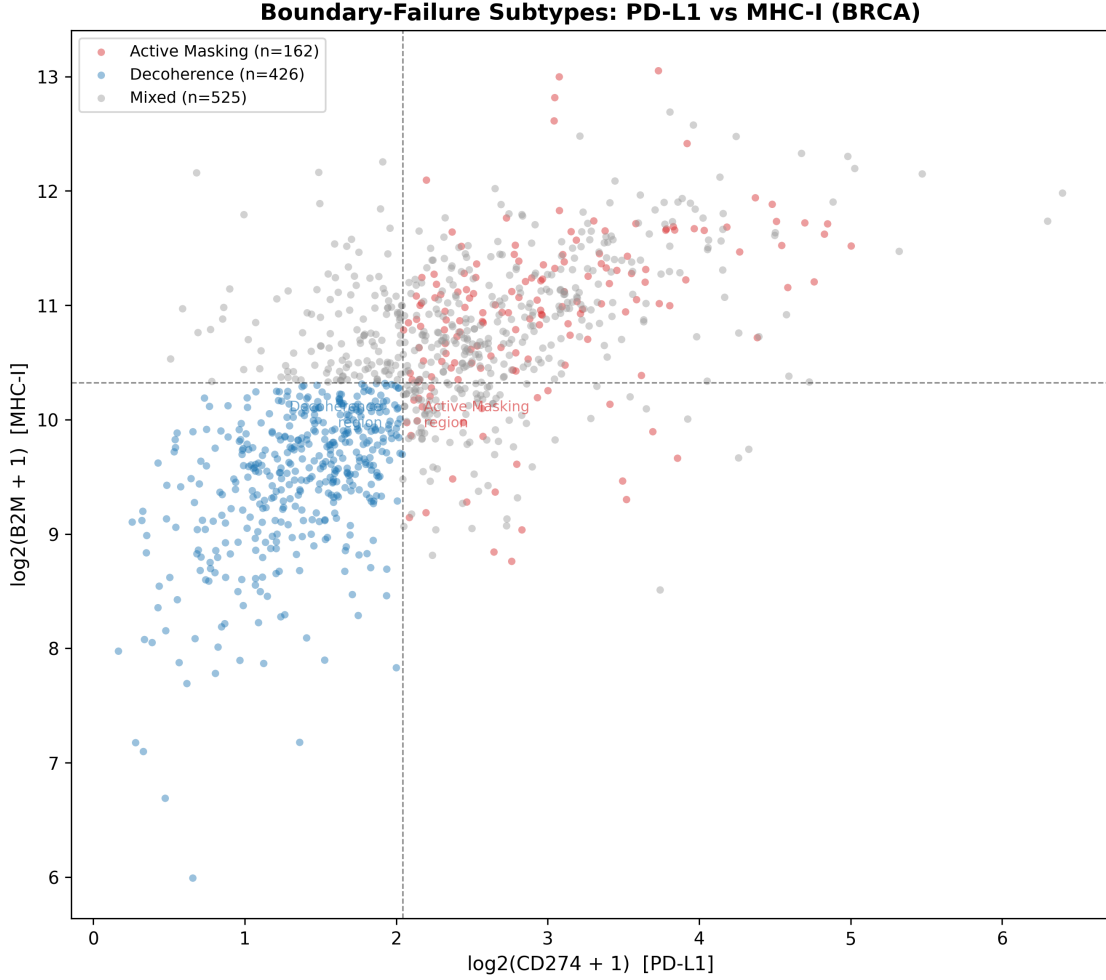


Figure 11: Checkpoint-clock boundary space colored by subtype classification. Active Masking and Decoherence occupy separable regions defined by PD-L1, ARNTL, PER1, and B2M threshold logic, illustrating the operational geometry of the subtype rule.

14.7 Survival Analysis

If the boundary-failure mode carries biological significance beyond gene-expression patterns, it should associate with clinical outcomes. We compared overall survival between Active Masking and Decoherence tumors using Kaplan–Meier analysis with log-rank tests on a patient-level deduplicated cohort (one tumor sample per case). Because TCGA does not provide immunotherapy response endpoints and treatment is heterogeneous, these are natural-history associations rather than evidence of checkpoint-blockade efficacy.

Active Masking tumors showed better overall survival than Decoherence tumors in the following pattern:

- TCGA-SKCM: log-rank $p = 0.0011$, BH $q = 0.0132$ (significant; Active Masking survives longer)
- TCGA-LUAD: log-rank $p = 0.049$, BH $q = 0.294$ (same direction, nominal only)

- TCGA-BRCA, TCGA-COAD, TCGA-HNSC, TCGA-LUSC: not significant

Across the 12 pre-specified cohort-level survival contrasts (6 AM-vs-DC and 6 circadian quartile tests), BH correction across all 12 tests yields 1 FDR-significant endpoint (SKCM AM-vs-DC), 1 nominal endpoint (LUAD AM-vs-DC), and 10 non-significant endpoints.

Threshold sensitivity. To test whether the melanoma survival signal depends on the specific median-split threshold, we swept the classification percentile from 25th to 75th in steps of 5 and re-ran AM-vs-DC log-rank tests at each threshold. The SKCM signal is significant ($p < 0.05$) from the 25th to the 65th percentile (9/11 thresholds), with the strongest signal at the 35th–40th percentile ($p = 0.0005$). The median (50th percentile) is therefore a conservative choice, not a cherry-picked threshold. LUAD reaches nominal significance only at the median. Figure 12 shows $-\log_{10}(p)$ across thresholds.

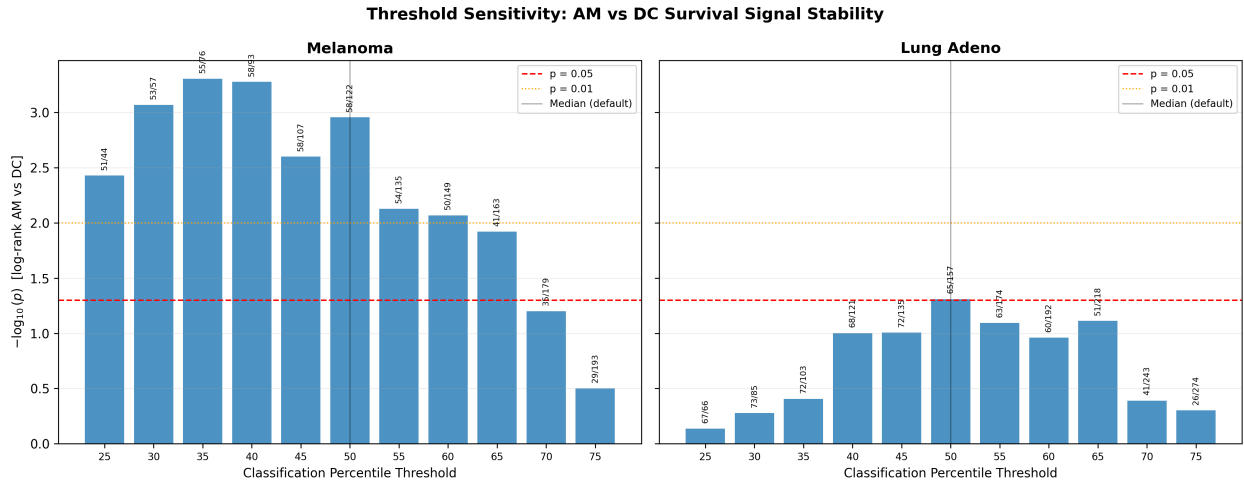


Figure 12: Threshold sensitivity sweep: AM-vs-DC log-rank p across classification percentile thresholds (25th–75th). SKCM is significant at 9/11 thresholds (strongest at 35th–40th percentile, $p = 0.0005$). The default median split is conservative. Annotated fractions show n_{AM}/n_{DC} at each threshold.

Quartile-based circadian CV alone did *not* predict survival in any of the six cancer types (Figure 14), suggesting that boundary-failure *mode* may matter more than coherence level per se. A tumor with low circadian CV is not inherently better or worse; what matters is *why* its clock is coherent. Active Masking tumors (coherent clock + checkpoint engagement) are plausibly more immune-visible, while Decoherence tumors (disordered clock + antigen loss) are plausibly more immune-evasive. Clinical-adjusted robustness models are reported in Section 14.8.

Kaplan-Meier Survival: Active Masking vs Decoherence

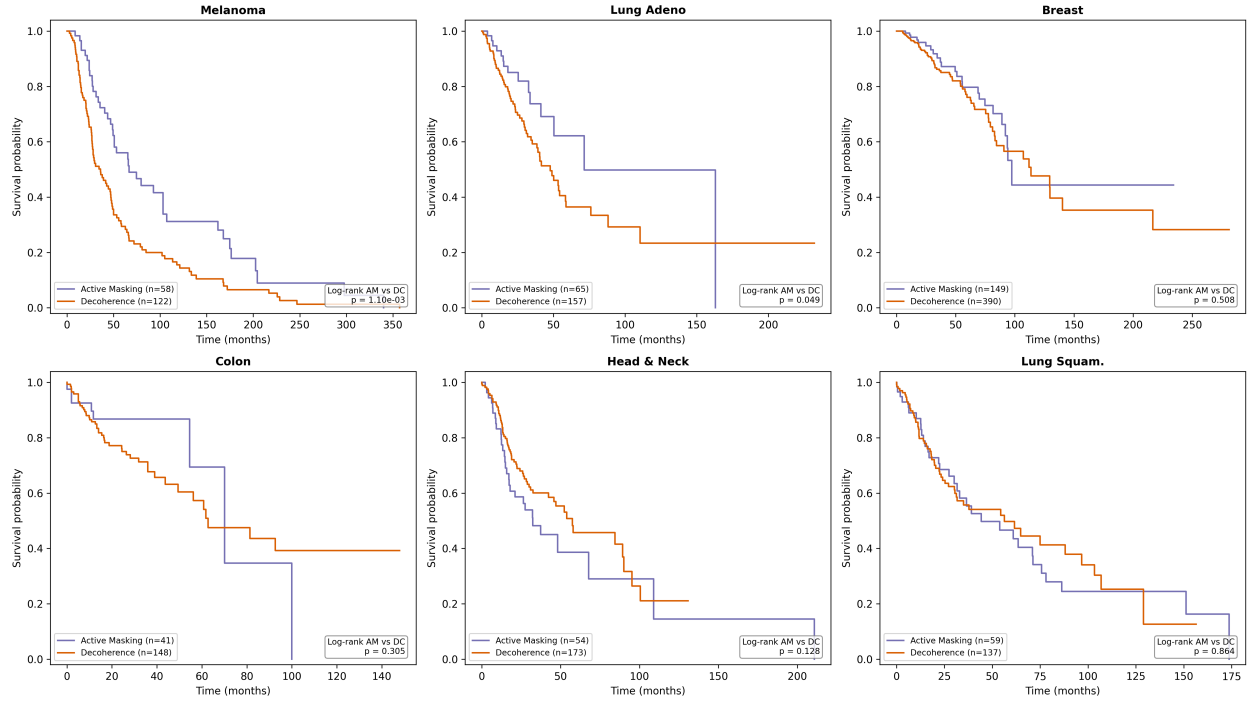


Figure 13: Kaplan-Meier survival curves by boundary-failure subtype in the patient-level deduplicated cohort. Active Masking shows better overall survival than Decoherence in SKCM (log-rank $p = 0.0011$, BH $q = 0.0132$ across all 12 survival tests) and a directionally similar nominal trend in LUAD ($p = 0.049$, $q = 0.294$); the remaining four cohorts are non-significant.

Kaplan-Meier Survival by Circadian Coherence Quartile

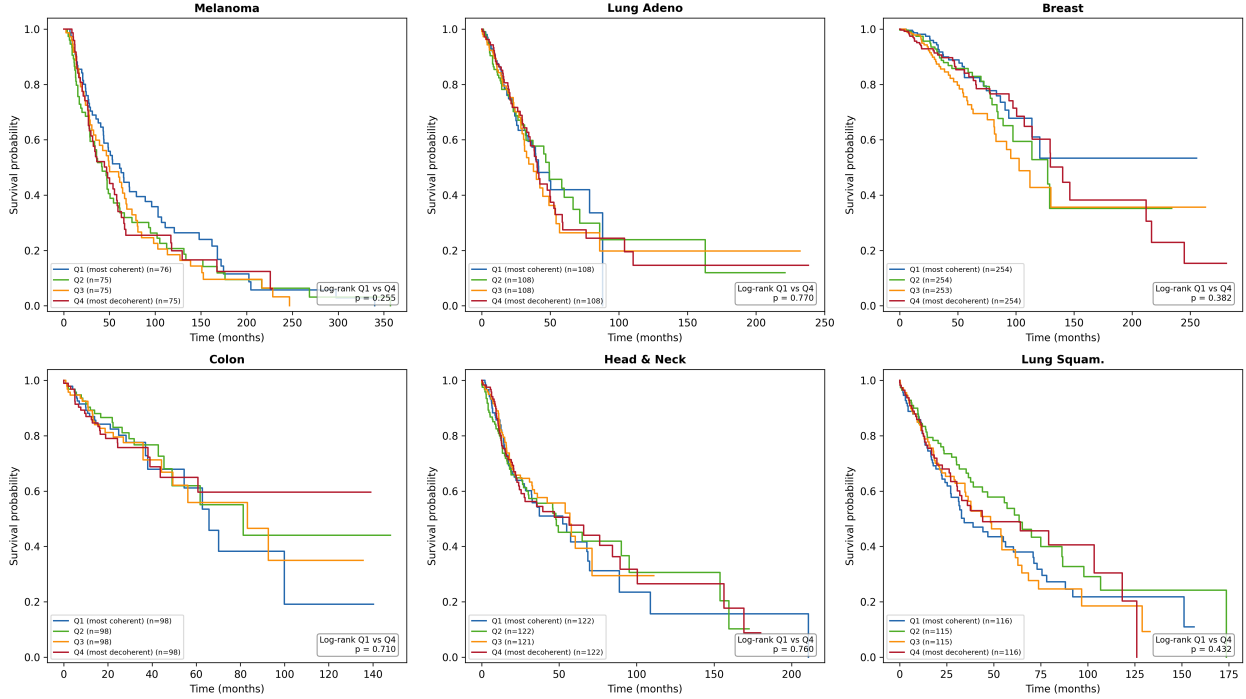


Figure 14: Kaplan-Meier curves by circadian-CV quartiles (Q1 most coherent to Q4 most decoherent) across the six TCGA cohorts. No cohort reaches FDR significance for Q1-vs-Q4 log-rank tests, indicating that coherence level alone is weaker than boundary-mode stratification for survival association in this dataset.

14.8 Robustness to Clinical Covariates and Interaction Structure

To reduce confounding risk from clinical composition, we re-estimated the survival signal in SKCM and LUAD using multivariable Cox models in the deduplicated patient-level cohort (one tumor sample per case). Covariates included boundary mode, age, sex, and stage as categorical indicators (II/III/IV plus stage-missing, with stage I as reference). When available, we added microenvironment covariates from the TCGA immune landscape characterization [47] (purity, lymphoid/myeloid/leukocyte infiltration proxies, stromal fraction, IFN- γ response, and TGF- β response). We tested a continuous interaction term between PD-L1 and an orthogonal clock metric (circadian CV computed from CLOCK, PER2, CRY1, and CRY2, excluding ARNTL/PER1 to reduce definitional coupling). We also ran a sensitivity model that adds continuous PD-L1 and B2M terms to test whether boundary mode adds signal beyond these components. Primary robustness tests were BH-corrected across cohorts and tests.

- **Adjusted boundary-mode effect:** In the microenvironment-adjusted Cox model, Active Masking remained associated with lower hazard in both cohorts, but FDR support differed: SKCM HR = 0.507, $p = 0.0286$, BH $q = 0.0686$ (nominal), LUAD HR = 0.288, $p = 0.0114$, BH $q = 0.0454$ (FDR-significant).

- **Adds beyond PD-L1/B2M sensitivity:** After adding continuous PD-L1 and B2M to the adjusted model, boundary mode remained directionally protective but was no longer FDR-significant in either cohort (SKCM HR = 0.562, $p = 0.131$, $q = 0.174$; LUAD HR = 0.273, $p = 0.0343$, $q = 0.0686$).
- **PD-L1 × clock interaction:** The continuous interaction term was significant in SKCM (HR = 0.217, $p = 0.00749$, BH $q = 0.0454$), supporting non-additive coupling between checkpoint engagement and orthogonal clock state. The interaction was not significant in LUAD ($p = 0.240$, $q = 0.274$).
- **Within high PD-L1 tumors:** The orthogonal clock main effect was non-significant in both cohorts (SKCM $p = 0.276$; LUAD $p = 0.0785$), indicating that clock contribution is not a uniform marginal effect in checkpoint-high strata.
- **Partial-correlation controls:** The circadian CV–PD-L1 association remained negative after adjusting for available control covariates (SKCM partial $r = -0.238$, $p = 4.29 \times 10^{-5}$; LUAD partial $r = -0.144$, $p = 0.00658$). Using the orthogonal clock metric, this adjusted association was strong in LUAD (partial $r = -0.269$, $p = 2.52 \times 10^{-7}$) and weaker/non-significant in SKCM ($p = 0.105$), indicating cohort-dependent robustness.

These robustness analyses remain observational and complete-case. Covariate availability reduced model sample sizes (for example, AM-vs-DC models used $n = 175$ in SKCM and $n = 183$ in LUAD). Figure 16 summarizes hazard-ratio estimates and confidence intervals across pre-specified robustness models. Time-interaction proportional-hazards screens indicated broad potential non-proportionality across covariates. Cox coefficients should therefore be interpreted as time-averaged associations pending stratified or explicitly time-varying follow-up models.

Restricted Mean Survival Time (RMST). Because PH violations are prevalent in the Cox models, we computed RMST (area under the KM curve up to a time horizon τ) as a PH-assumption-free alternative. RMST difference (AM minus DC) with bootstrap 95% CIs ($n = 1,000$ resamples):

- SKCM ($\tau = 60$ months): +11.3 months (95% CI: 5.3–16.8); ($\tau = 120$ months): +24.2 months (95% CI: 10.8–36.8). Significant at all four time horizons tested.
- LUAD ($\tau = 60$ months): +7.8 months (95% CI: 1.3–14.2). Significant up to $\tau = 84$ months; 120-month CI crosses zero due to sparse late follow-up.

The AM survival advantage in melanoma is confirmed without any proportional hazards assumption. Figure 15 shows RMST differences with bootstrap CIs.

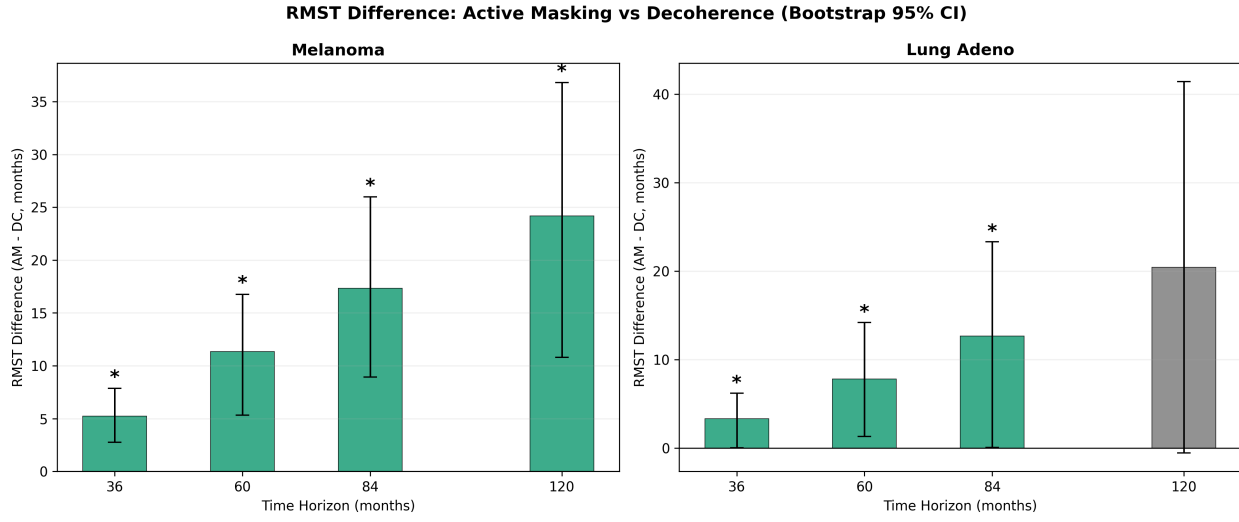


Figure 15: RMST difference (Active Masking minus Decoherence, in months) at four time horizons for SKCM and LUAD. Bootstrap 95% CIs ($n = 1,000$, seed=42). Green bars: CI excludes zero (significant). The PH-free RMST confirms the AM survival advantage at every horizon in melanoma.

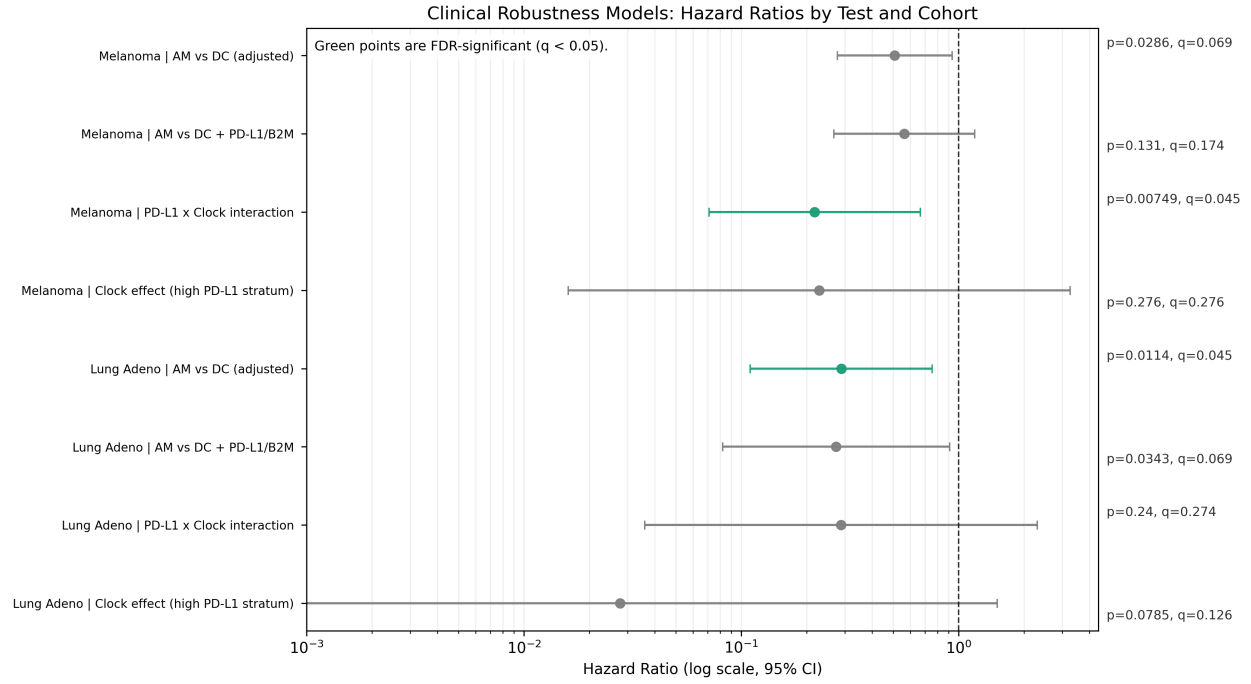


Figure 16: Hazard-ratio forest plot for primary robustness models in SKCM and LUAD. Points show Cox HR estimates with 95% confidence intervals; green markers denote FDR-significant tests. Two tests meet FDR significance (LUAD adjusted AM-vs-DC and SKCM PD-L1 \times Clock interaction), while the remaining primary tests are nominal or non-significant.

14.9 Stage-Stratified Analysis

To determine whether circadian restructuring is an early or late event in tumor progression, we tested the association between circadian CV and pathologic tumor stage across all six cancer types.

Circadian CV was **largely stage-stable**: 11/12 circadian-stage tests were non-significant after global FDR correction, with one near-threshold HNSC Spearman trend ($q = 0.04998$, $\rho = 0.112$; technically FDR-significant but small in magnitude). This pattern remains more consistent with an early-established, persistent circadian restructuring state than with a strong late-stage accumulation effect. However, these associations do not by themselves establish temporal ordering or causality. (Other non-circadian markers, such as CD274/B2M and gap-junction summaries in specific cohorts, showed modest stage associations after global FDR correction.)

This pattern is compatible with the framework's prediction that boundary failure can be a foundational event, a shift in the cell's relationship with the organism, rather than only a downstream consequence of tumor burden. It motivates, but does not yet establish, the use of circadian-based biomarkers for early disease settings. Figure 18 shows the corresponding Spearman trend effects and BH-adjusted q values.

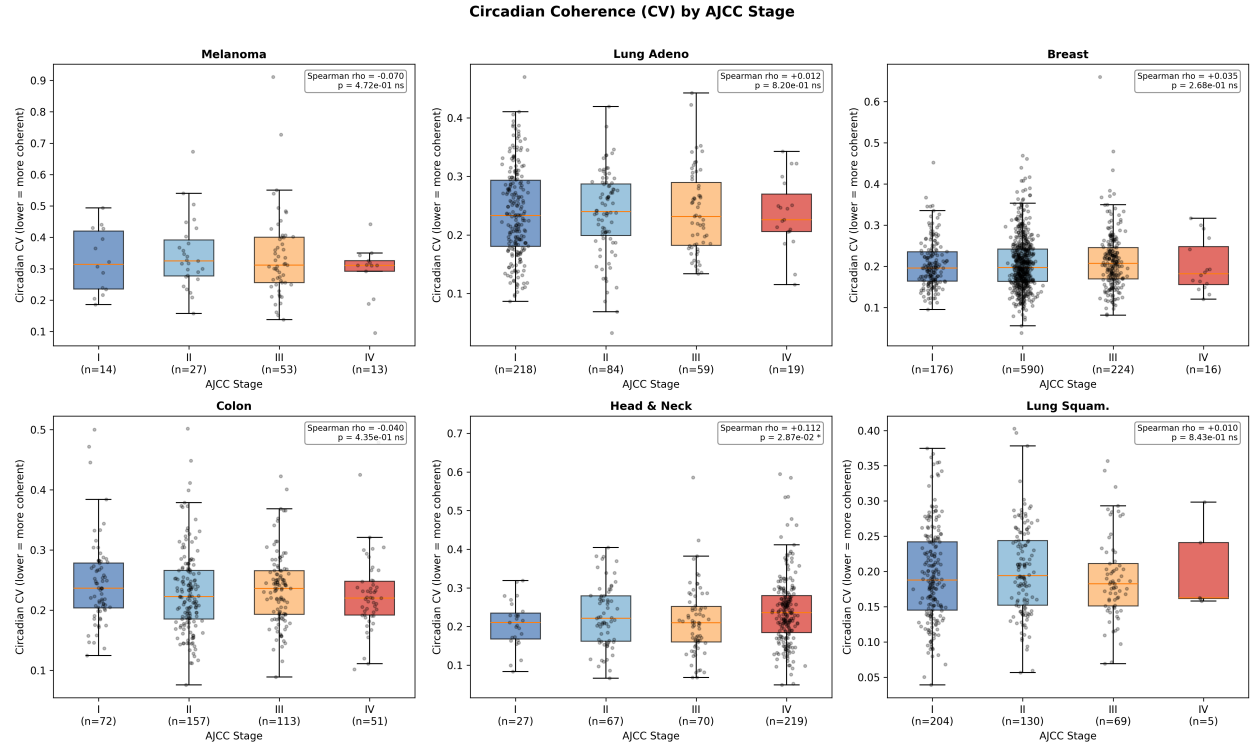


Figure 17: Circadian CV by pathologic tumor stage across six TCGA cancer types. Circadian-stage association is largely absent after global FDR correction, with one near-threshold HNSC trend ($q = 0.04998$, small effect size), consistent overall with stage-stable circadian restructuring.

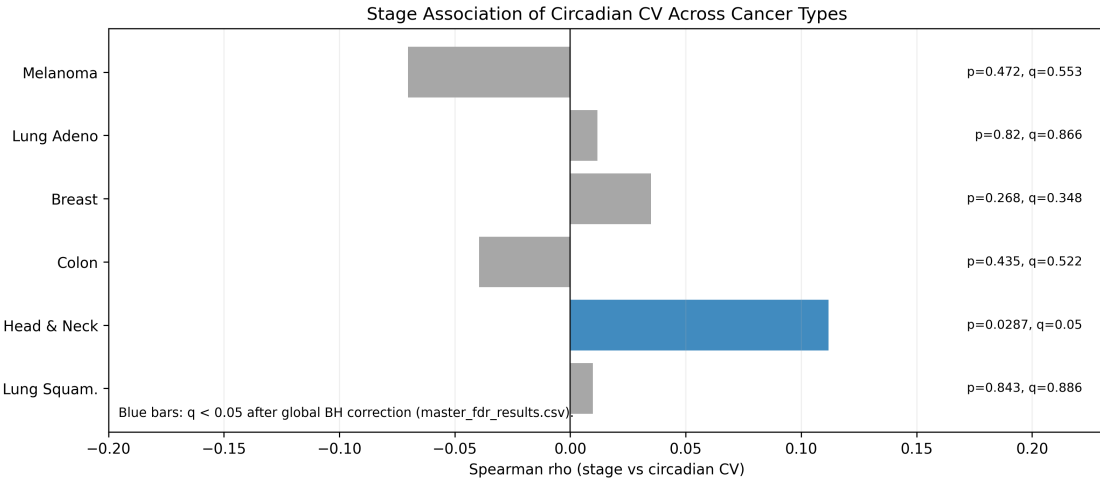


Figure 18: Spearman stage-trend effect sizes for circadian CV across all six cohorts. q-values are taken from the global BH correction table (`master_fdr_results.csv`); most effects are near zero/non-significant, with one near-threshold HNSC signal ($q = 0.04998$, $\rho = 0.112$), reinforcing a largely stage-stable circadian signal in this dataset.

14.10 Stromal Confound Sensitivity

A key alternative explanation for the circadian CV–PD-L1 coupling is that immune cell infiltration drives both signals: interferon- γ from T cells co-activates PD-L1 and BMAL1-responsive programs [47], so the “locked clock” could reflect immune cell admixture rather than tumor-intrinsic restructuring. We addressed this with two complementary analyses.

Immune-fraction residualization. We regressed circadian CV on five immune covariates (leukocyte fraction, lymphocyte infiltration, IFN- γ response, tumor purity, stromal fraction) from the Thorsson et al. immune landscape data [47] and correlated the residual CV with PD-L1. Immune covariates explained only 0.7–13.8% of circadian CV variance (R^2). After removing these effects, the residual CV–PD-L1 correlation remained significant in all four cohorts tested: SKCM (residual $\rho = -0.141$, $p < 0.01$), LUAD ($\rho = -0.159$, $p < 0.001$), BRCA ($\rho = -0.173$, $p < 0.001$), and HNSC ($\rho = -0.126$, $p < 0.01$). Figure 19 shows the residualized scatter.

Purity-stratified replication. We split tumors into purity tertiles and re-computed the CV–PD-L1 correlation within each stratum. The negative correlation persisted within all three tertiles for SKCM (strongest in Low purity: $\rho = -0.480$), LUAD, and BRCA (9/9 tertile-level tests significant in these cohorts). HNSC tertiles were individually non-significant, consistent with its smallest raw effect size ($\rho = -0.125$ overall). Figure 20 shows the stratified correlations.

These analyses do not rule out all immune confounding (single-cell resolution is required for that), but they demonstrate that the circadian–checkpoint coupling has a component beyond bulk immune-fraction mixing.

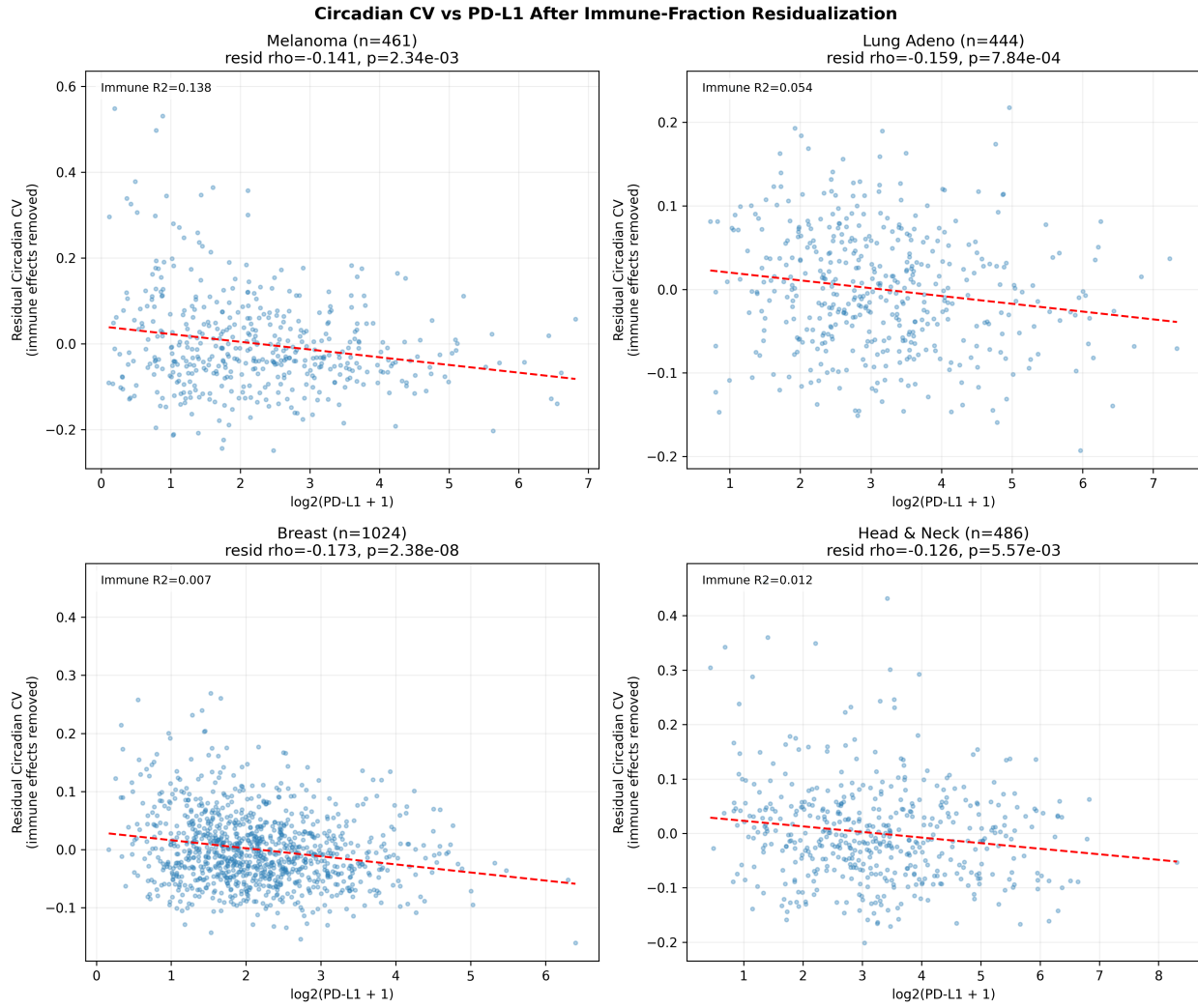


Figure 19: Circadian CV vs. PD-L1 after immune-fraction residualization in four TCGA cohorts. Immune covariates explain $R^2 = 0.007\text{--}0.138$ of CV variance; the residual CV–PD-L1 correlation remains significant in all four cohorts.

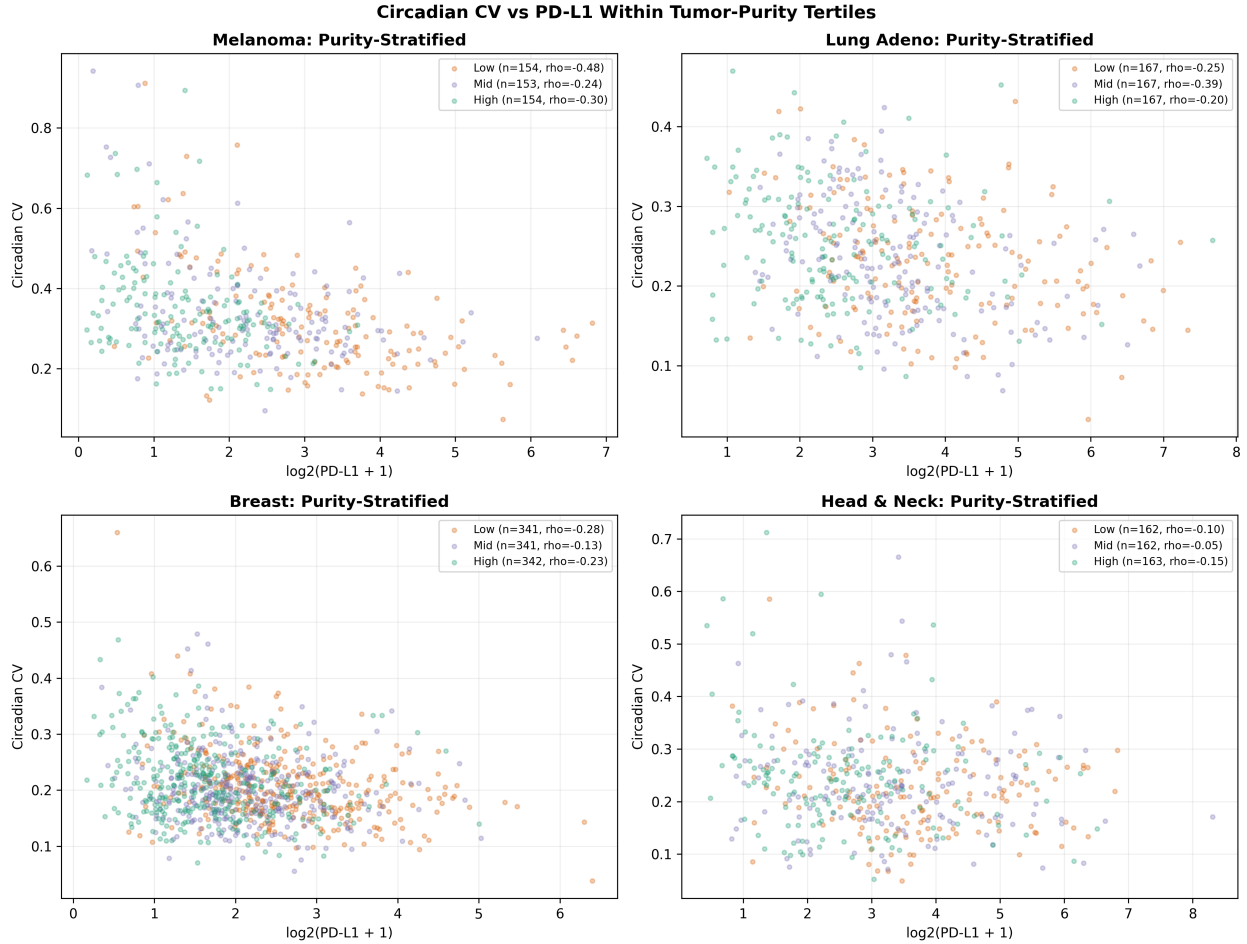


Figure 20: Circadian CV vs. PD-L1 within tumor-purity tertiles. The negative correlation persists in all three strata for SKCM, LUAD, and BRCA, arguing against a pure stromal-mixing explanation.

14.11 Composite Observability Index

To address the concern that “forced distinction” risks tautology (cancer = loss of distinction, therapy = restoration of distinction), we constructed an independent composite observability index from features *not* used in the AM/DC classification rule:

- MHC-I composite: mean $\log_2(\text{HLA-A}, \text{HLA-B}, \text{HLA-C})$ —not B2M (used in DC definition)
- Gap junction composite: mean $\log_2(\text{GJA1}, \text{GJB2}, \text{GJA5}, \text{GJB6})$ —not used in AM/DC at all
- Orthogonal circadian CV: CV of CLOCK, PER2, CRY1, CRY2—excluding ARNTL and PER1 (used in AM definition)

Each component was z -scored within cohort and averaged with equal weights (higher index = more observable).

The index separates AM from DC with $p = 1.7 \times 10^{-10}$ (SKCM) and $p = 1.5 \times 10^{-20}$ (LUAD), confirming that boundary-failure subtypes differ on features independent of their definition. It correlates with PD-L1 at $\rho = +0.482$ (SKCM) and $+0.539$ (LUAD). Median-split survival shows a directional advantage for high-observability tumors ($p = 0.063$ SKCM, $p = 0.083$ LUAD)—not FDR-significant, but consistent with the framework using deliberately weaker/orthogonal features. Figure 21 shows the survival comparison.

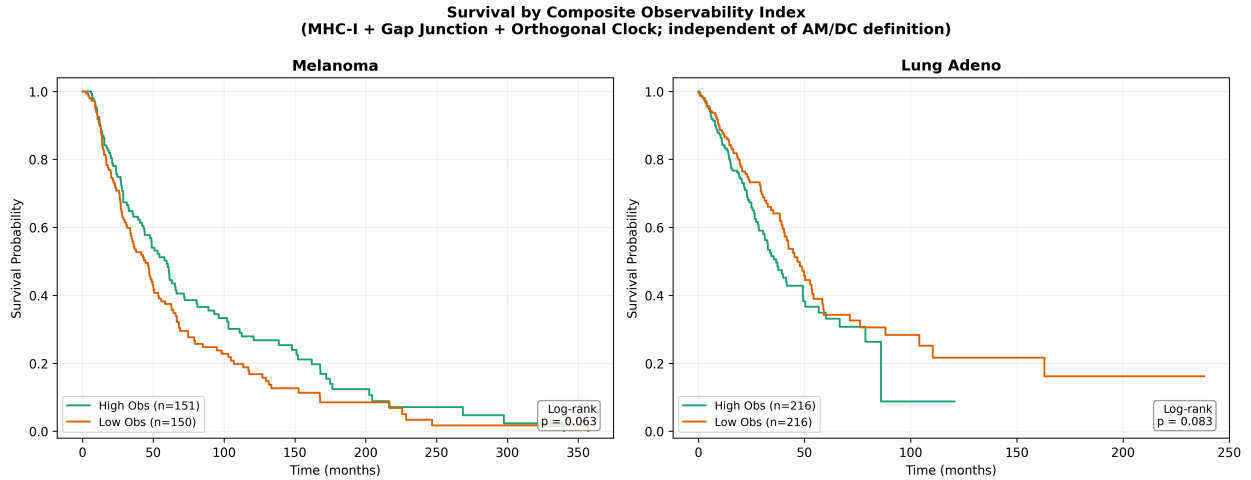


Figure 21: Kaplan-Meier survival by composite observability index (median split) in SKCM and LUAD. The index uses features independent of the AM/DC classification rule (HLA-A/B/C, gap junctions, orthogonal clock genes). Directional survival advantage for high-observability tumors is consistent with the framework.

14.12 External Validation: GSE91061 (Nivolumab Melanoma)

To test generalizability beyond TCGA, we analyzed pre-treatment melanoma RNA-seq data from an independent nivolumab immunotherapy cohort (GSE91061; Riaz et al., 2017 [49]; $n = 49$ pre-treatment samples with known response: 10 PR/CR, 16 SD, 23 PD). Gene expression (FPKM) was available for all 15 target genes via Entrez ID mapping.

The circadian CV–PD-L1 negative correlation **replicates** in this independent cohort: Spearman $\rho = -0.283$, $p = 0.049$. This is the seventh cohort showing the same direction (7/7 negative across 6 TCGA + 1 external). Among responders (PR/CR), mean circadian CV was 0.300 vs. 0.350 for progressors (PD), consistent with the framework’s prediction that lower CV tracks immune-engaged boundary states.

AM-vs-DC response rate comparison (Fisher exact $p = 1.0$; $n_{\text{AM}} = 10$) is underpowered for a subtype-level response-rate test and is reported as descriptive. Adequate power for the prospective prediction (AM responds better to checkpoint blockade) requires larger immunotherapy cohorts. Figure 22 shows the three-panel external validation summary.

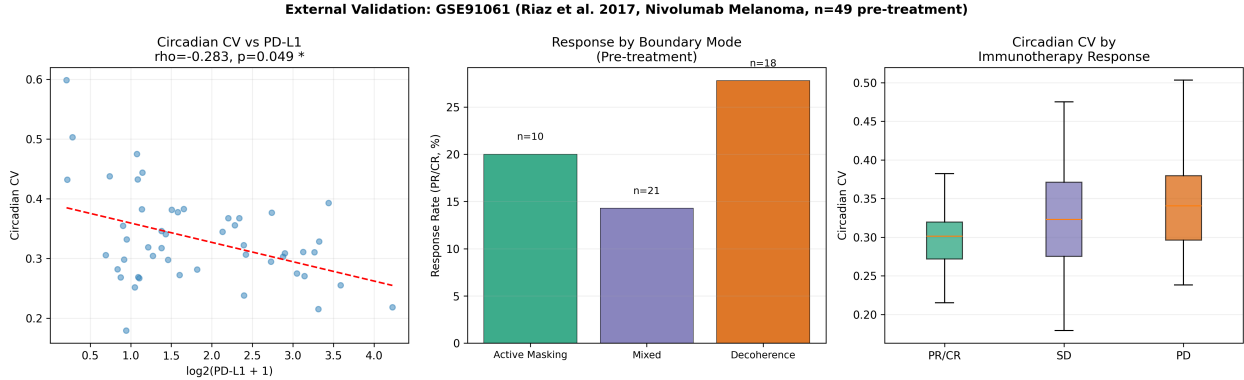


Figure 22: External validation in GSE91061 (Riaz et al., nivolumab melanoma, $n = 49$ pre-treatment). Left: circadian CV vs. PD-L1 replicates the TCGA negative correlation ($\rho = -0.283, p = 0.049$). Center: immunotherapy response rate by boundary-failure subtype (underpowered, descriptive). Right: circadian CV by RECIST response category (responders show lower CV).

14.13 Implications for the Framework

The expanded TCGA analysis across six cancer types and $n = 3,611$ tumors, supplemented by sensitivity analyses and one external cohort, refines the boundary-failure framework in the following ways:

1. **Boundary failure is not monolithic.** The data confirm at least two distinct failure modes across all six cancer types: (a) *Active Masking*, where the tumor retains a low-CV (transcriptionally “locked”) clock-gene signature and deploys checkpoint molecules to veto organism-level clearance (visible but vetoed), and (b) *Temporal Decoherence*, where clock-gene structure is more variable and immune visibility is low (invisible). Both are boundary failures, but through different mechanisms with different clinical implications.
2. **The clock is transcriptionally locked, not uniformly disordered.** Tumors show lower circadian CV than matched normals in 4/5 cancer types (with one non-significant cohort, COAD), and Active Masking tumors show the lowest CV of all. This is inconsistent with a simple “broken clock” expectation for bulk clock-gene expression and supports clock co-option in this proxy.
3. **Budget Escape, not Trade-off.** Contrary to a simple resource trade-off hypothesis, proliferation and coherence markers show positive correlation in 5/6 cancer types. This contradicts a fixed-budget constraint within the tumor ($C_G + C_S \leq B$) and supports a “budget escape” model where malignant cells expand metabolic capacity (Warburg effect) to sustain both high proliferation and high internal order, externalizing the cost to the host (cachexia).
4. **Boundary-failure mode is associated with survival heterogeneity.** Active Masking tumors show better overall survival than Decoherence tumors in melanoma (significant

after BH correction across all 12 survival tests: $p = 0.0011$, $q = 0.0132$), with a directionally similar but nominal result in lung adenocarcinoma ($p = 0.049$, $q = 0.294$). In multi-variable, microenvironment-adjusted Cox robustness models (SKCM/LUAD), boundary-mode effects remained protective in both cohorts, FDR-significant in LUAD ($\text{HR} = 0.288$, $q = 0.0454$) and nominal in SKCM ($\text{HR} = 0.507$, $q = 0.0686$); PD-L1 \times orthogonal-clock interaction was significant in SKCM ($\text{HR} = 0.217$, $q = 0.0454$).

5. **Circadian restructuring is largely stage-stable in this dataset.** Most circadian-stage tests were non-significant after global FDR correction, with one near-threshold HNSC trend ($q = 0.04998$, $\rho = 0.112$). This is compatible with early establishment and persistence but does not alone establish temporal causality.
6. **The circadian–checkpoint coupling survives stromal confound tests.** After regressing out immune-infiltration covariates, the residual CV–PD-L1 correlation remains significant in 4/4 cohorts tested (R^2 of immune effects on CV: 0.7–13.8%). Within-purity-tertile replication further argues against a pure stromal-mixing artifact (Section 14.10).
7. **Independent operationalization of “observability.”** A composite index constructed from features orthogonal to the AM/DC classification rule separates the subtypes with $p < 10^{-10}$ and correlates with PD-L1 at $\rho > 0.48$, demonstrating that boundary-failure mode captures real biology beyond definitional artifacts (Section 14.11).
8. **External replication.** The circadian CV–PD-L1 negative correlation replicates in an independent nivolumab melanoma cohort (GSE91061; $\rho = -0.283$, $p = 0.049$), extending the finding to 7/7 cohorts tested (Section 14.12).
9. **Hypothesis-generating therapeutic implications.** The Active Masking / Decoherence distinction motivates different therapeutic strategies to test prospectively: checkpoint-based approaches may preferentially benefit Active Masking-like states (restore a vetoed immune response), while Decoherence-like states may require differentiation or antigen-restoration strategies before checkpoint blockade. Gap junction expression remains an unreliable RNA-level proxy for functional GJIC; functional assays are required.

15 Simulation

We include a simple simulation (Appendix A) to demonstrate the qualitative behavior implied by the boundary-failure hypothesis. The simulation is not calibrated to real tumors; it is designed to show a failure mode.

15.1 Update Rules

At each discrete time step, each node:

1. Consumes energy ϵ_i from a global control budget $B_{\text{homeostasis}}$ (a coarse proxy for host resources and control capacity; cf. Eq. 8).
2. May mutate from Healthy to PreCancer (with small probability).

3. May progress from PreCancer to Cancer with a corresponding drop in alignment p_i .
4. If cancerous, loses a subset of regulatory edges (decoupling from SIG and TMP).
5. Divides with probability proportional to r_i ; healthy nodes are subject to a contact-inhibition proxy (maximum neighbor count) while cancerous nodes are not.

We record κ over time and track the cancer cell count. Under reasonable parameters, the system exhibits a transition from a high- κ , low-division regime to a low- κ , high-division regime once decoupled nodes appear.

15.2 What the Simulation Demonstrates

- Loss of signaling edges + self-referential proliferation \rightarrow coherence collapse
- Healthy cells self-regulate via contact inhibition; cancer cells do not
- Energy budget depletion accelerates as cancer cell count grows (Warburg effect proxy)
- The “crossing point” where κ decline and cell count acceleration meet represents the qualitative event horizon of the disease

Disclaimer: This is not a predictive cancer model. It does not capture genetics, metabolism, angiogenesis, immune editing, clonal heterogeneity, or spatial constraints. It demonstrates logical failure modes, not molecular causation.

Extended simulation framework: A modular Python implementation is available in the companion repository (github.com/MosesRahnama/cancer-paper-repository). It includes a simulation engine with history tracking, four therapeutic operators (forced distinction, differentiation therapy, checkpoint inhibition, bioelectric reprogramming), tissue-network visualization, and coherence-versus-cancer plotting. It implements the cancer transform operator (Section 10.3), the forced-distinction principle (Section 12), and a Warburg-proxy energy budget for end-to-end runs from healthy tissue through emergence, intervention, and post-intervention dynamics.

Calibrated monthly parameterization: To avoid an artificially vanishing pre-cancer dwell-time, we parameterize one simulation step as one month and map annual transformation risk to per-step probability via $p_{\text{step}} = 1 - (1 - r_{\text{annual}})^{1/12}$. Premalignant progression rates vary by lesion class [41]; for the illustrative oral epithelial dysplasia setting we use the pooled malignant transformation estimate $r_{\text{annual}} \approx 10.5\%$ [42], yielding $p_{\text{progression}} \approx 0.0092$. We pair this with $p_{\text{mutation}} = 0.002$ to represent persistent somatic mutation pressure in a toy setting [43]. In the companion code, the cancer energy multiplier ($\epsilon = 2.7$) is an illustrative Warburg-burden proxy for qualitative dynamics, not a fitted physiological constant.

Illustrative scenario comparison (extended framework): For one representative run (100 initial cells, seed=42, therapy applied at step 200), the calibrated model produces the following qualitative outcomes:

Therapy	Post-therapy κ	Cancer cells
No therapy (control)	0.418	376
Forced distinction	0.231	376
Differentiation therapy (ATRA-like)	0.441	0
Checkpoint inhibitor (anti-PD-1-like)	0.232	376
Bioelectric reprogramming (Levin-like)	0.199	376
Combination (Anti-PD-1 + ATRA)	0.441	0

These values are illustrative and parameter-dependent, not efficacy rankings. In this configuration, differentiation-like restoration reaches a halt state, while partial distinction-restoration operators increase observability without full clearance.

Figures 23, 24, 25, 26, and 27 visualize these trajectories from the companion codebase. The first two are generated by `python examples/run_full_scenario.py`; the latter three are generated by `python run_simulation.py`. Figure 28 and Figure 29 summarize multi-seed Phase-2 sweeps from `python run_phase2_extractions.py`. All outputs are written to `results/`.

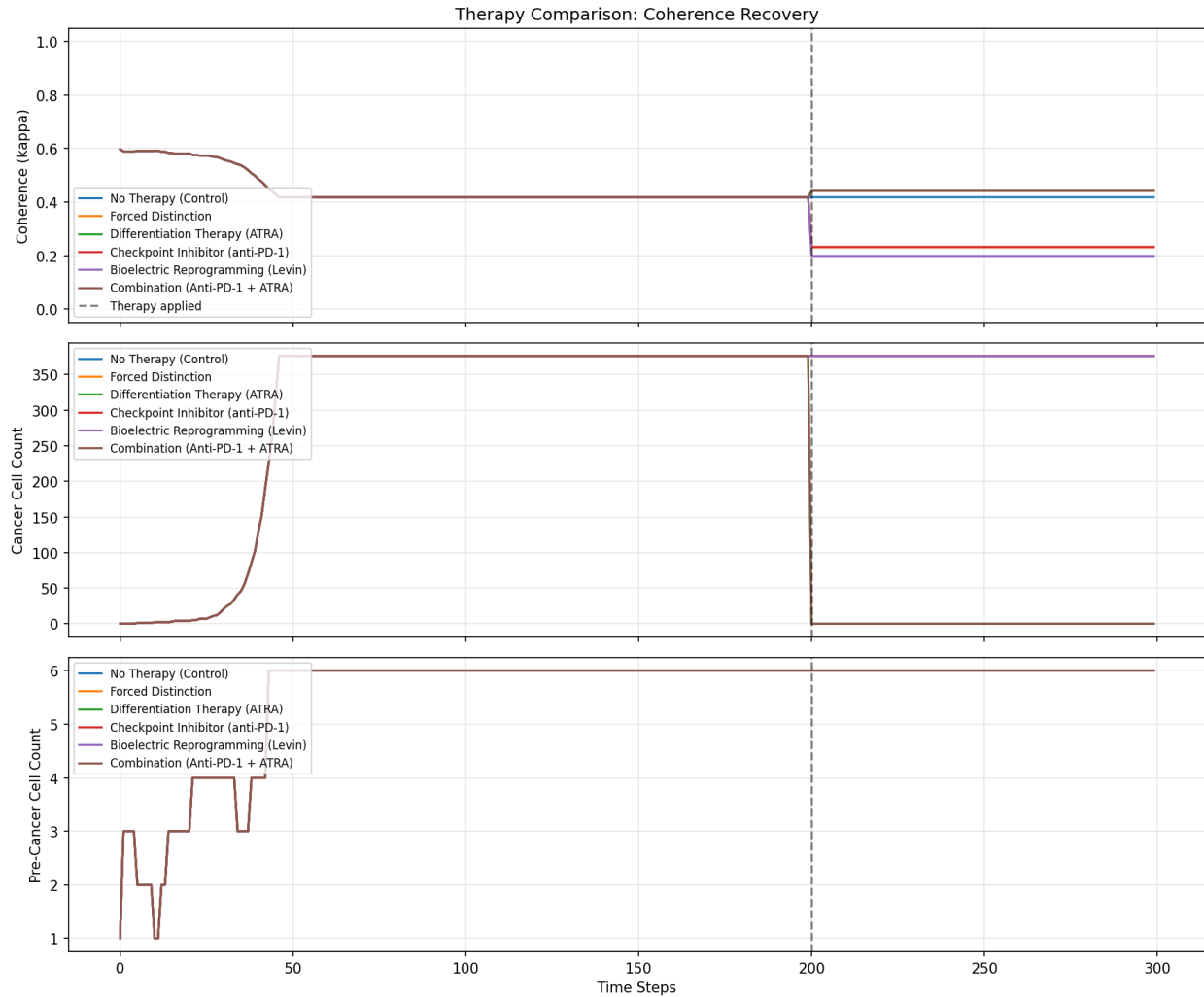


Figure 23: Extended simulation framework: coherence, cancer-count, and pre-cancer trajectories across five intervention strategies under the same initialization and seed.

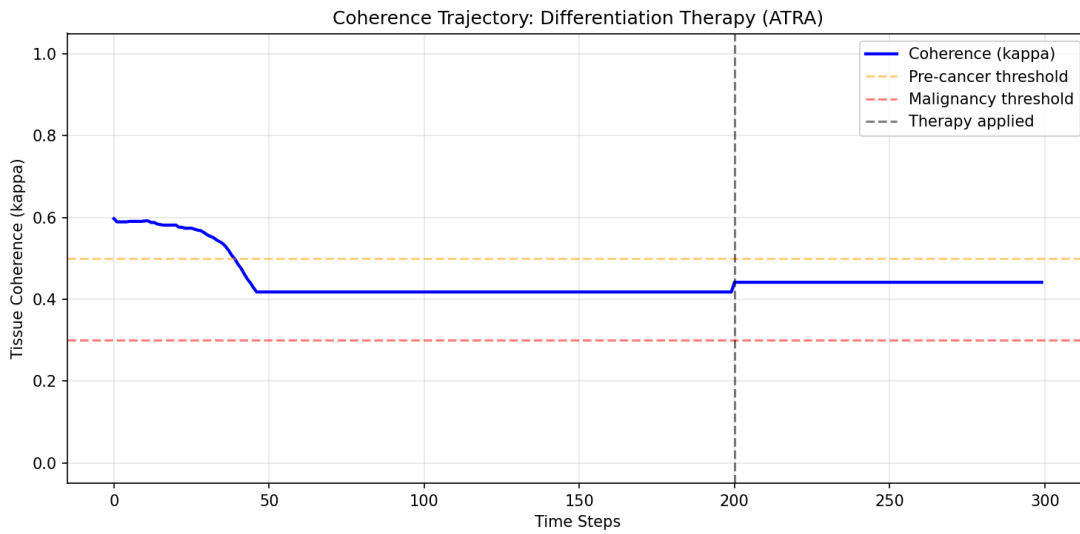


Figure 24: Single-therapy coherence trajectory (ATRA-like differentiation setting), showing post-intervention recovery in this illustrative run.

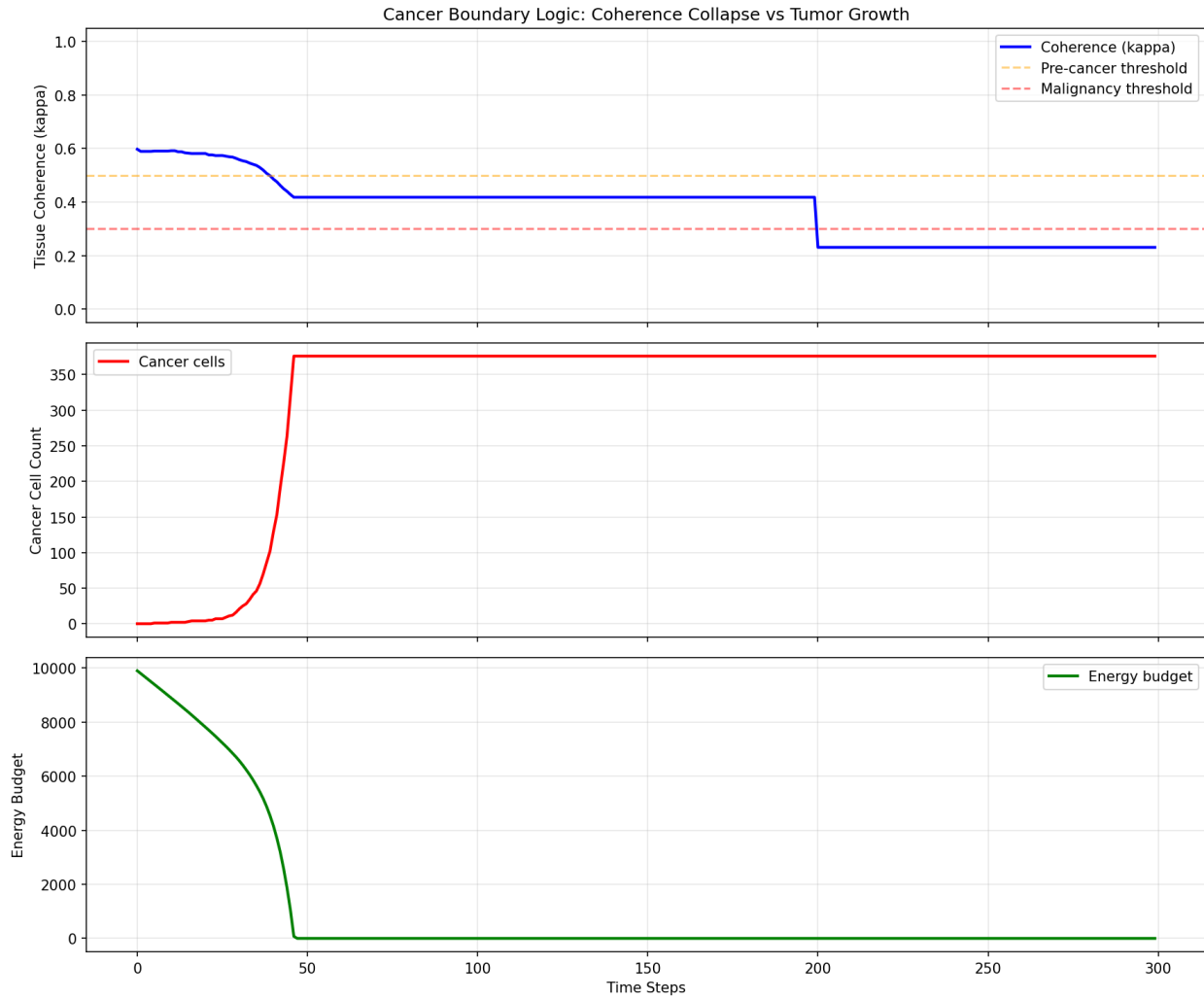


Figure 25: Reference simulation trajectory from `run_simulation.py`: coherence decline, cancer expansion, and energy-budget depletion over time.

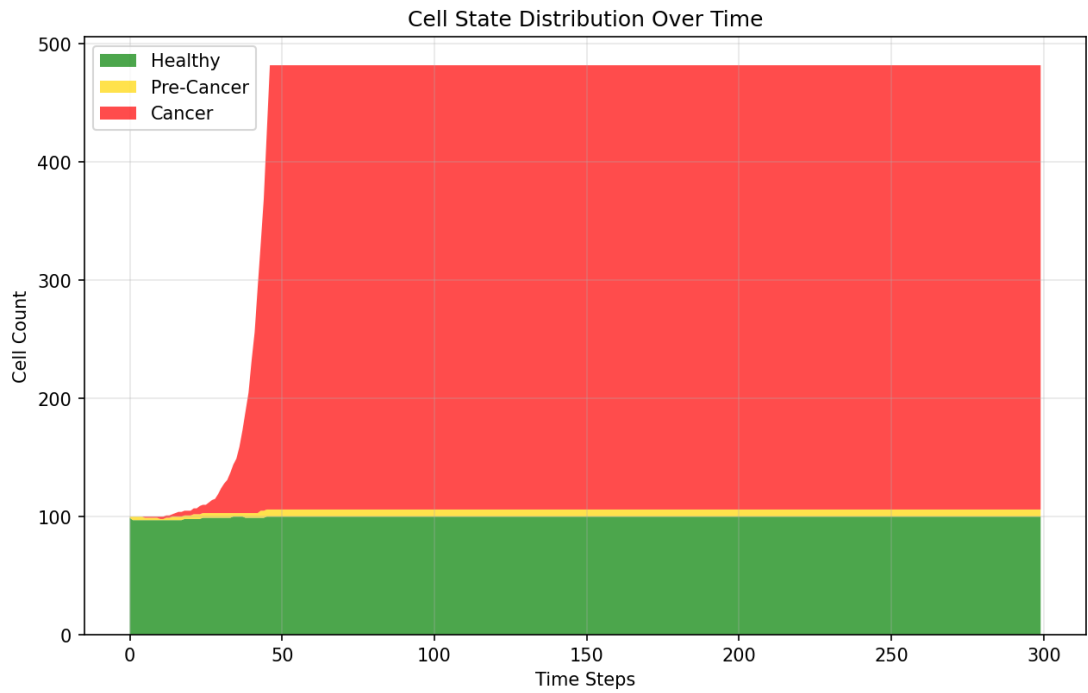


Figure 26: State distribution across simulation steps (healthy, pre-cancer, cancer), illustrating phase transitions in the toy tissue model.

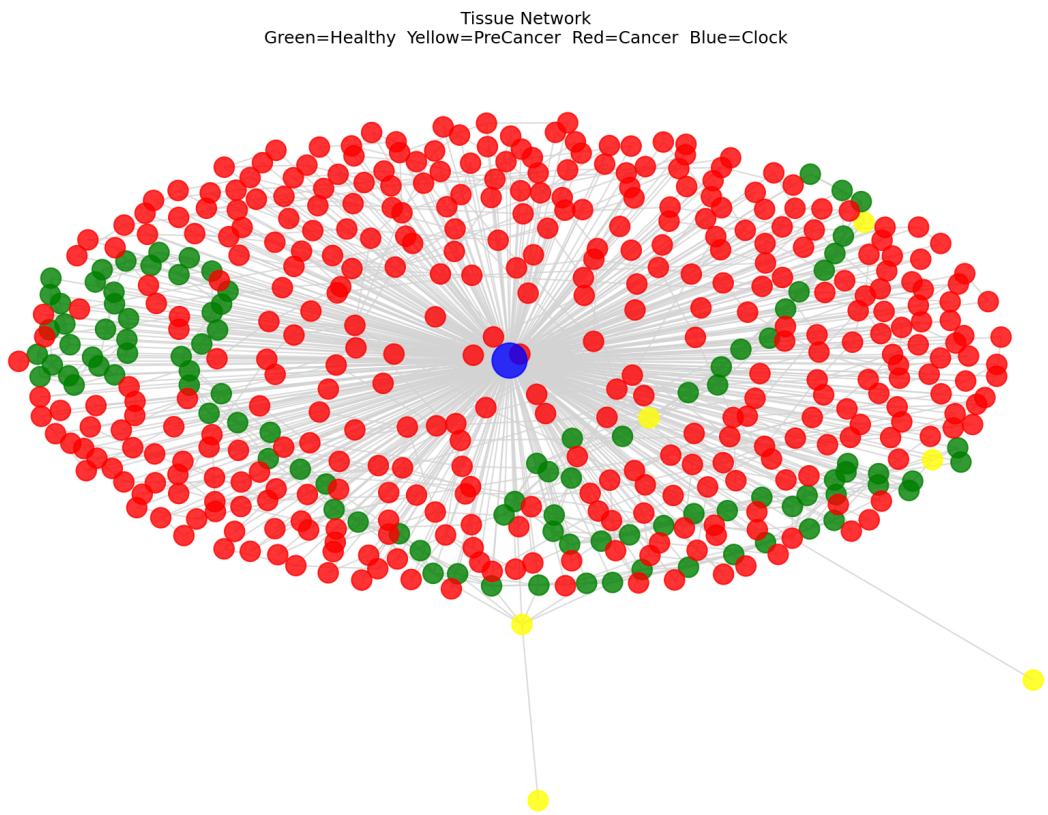


Figure 27: Representative tissue-network snapshot from the simulation, colored by cell state and showing local coupling structure.

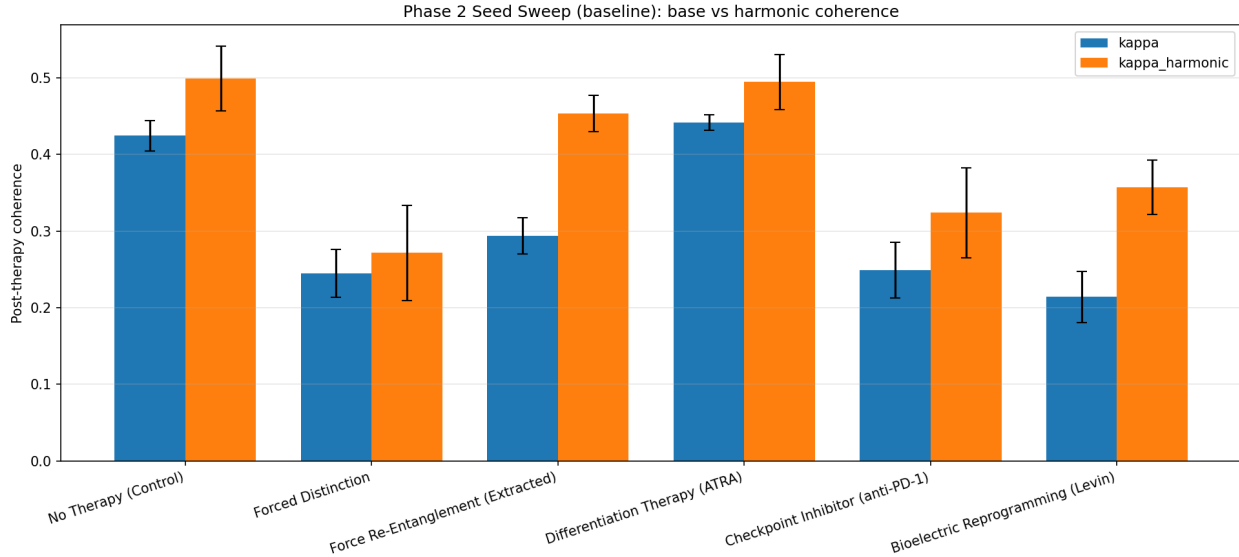


Figure 28: Phase-2 multi-seed sweep (baseline): post-therapy coherence summary for all operators under calibrated monthly parameters. Bars show mean and standard deviation across seeds for both base κ and harmonic-aware κ_{harmonic} variants.

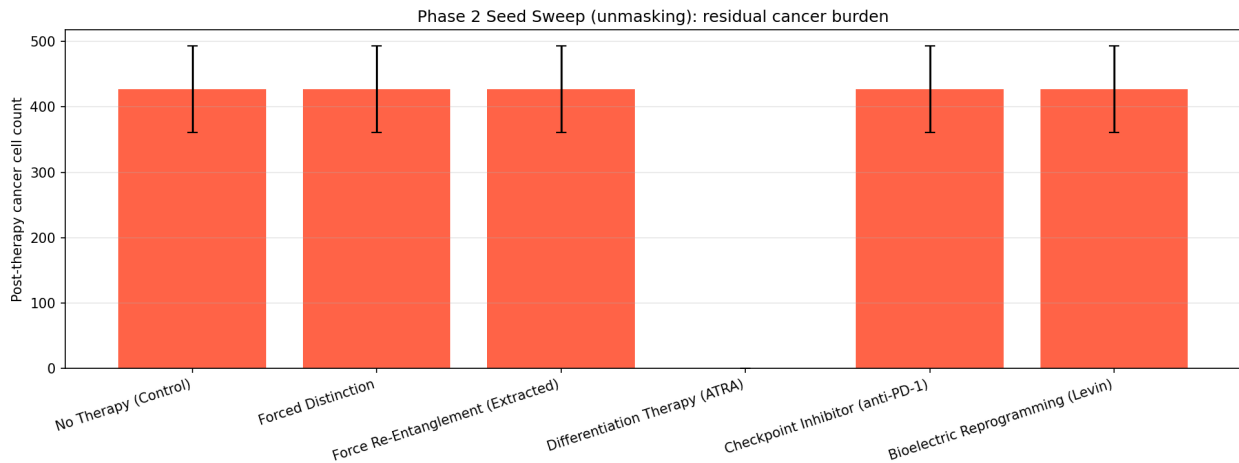


Figure 29: Phase-2 multi-seed sweep with unmasking stressor: residual post-therapy cancer burden across operators. Differentiation-like restoration remains the dominant clearance regime in this illustrative stress configuration.

16 Limitations

- **Model abstraction:** The graph variables p_i , edge labels, and κ are conceptual proxies. They are not directly mapped to specific molecular pathways. Operationalizing them requires the measurement program outlined in Section 11.

- **No genetics or heterogeneity:** The simulation does not capture mutational distributions, clonal selection, angiogenesis, invasion, or heterogeneity beyond a coarse state variable.
- **Parameter and seed dependence:** The main simulation figures use a single representative seed; initial multi-seed sweeps (20 seeds, Phase-2 extraction runner) are included but broader parameter sensitivity remains open.
- **No explicit immune-kill dynamics:** Immune recognition, clearance kinetics, and adaptive escape are not explicitly modeled. Some operators therefore change observability without automatically enforcing elimination.
- **Many endpoints are null or nominal:** Across pre-specified TCGA endpoint families, several contrasts are non-significant after correction (for example, most survival and stage-stratified tests). We report these explicitly and avoid treating nominal trends as confirmatory evidence.
- **External validation is preliminary:** The GSE91061 cohort ($n = 49$ pre-treatment) replicates the correlation-level finding but is underpowered for subtype-level response-rate comparisons. Larger immunotherapy cohorts with response endpoints are needed to test the prospective prediction that Active Masking tumors respond better to checkpoint blockade.
- **Subtype classification uses median splits:** The AM/DC threshold sensitivity sweep (9/11 percentile thresholds significant in SKCM) demonstrates robustness to threshold choice, but the classification remains a discretization of continuous expression space. Data-driven methods (e.g., Gaussian mixture models) may yield more biologically grounded boundaries.
- **Bulk RNA-seq does not resolve tumor-intrinsic vs. stromal signals:** Immune residualization and purity stratification mitigate but do not eliminate stromal confounding. Single-cell RNA-seq validation (particularly for clock-gene expression at cellular resolution) remains a critical next step.
- **Thermodynamics is interpretive:** While energy and information constraints motivate the narrative, we do not derive quantitative metabolic bounds from first principles. The Landauer framing is used as an organizing guide for distinguishing energetic replication cost from decoupled identity-forming processes; host metabolic burden and cachexia remain explicitly multi-mechanism processes.
- **Analogy boundaries:** `rec_succ` is used to clarify a structural failure mode (duplication without a termination predicate). It is not a claim of literal undecidability in biology.
- **Identity-weight abstraction:** The variables w_{self} , w_{org} , and $A(t)$ are coarse control proxies. Operational mappings to specific molecular observables require dedicated calibration.
- **Control-budget constraint:** Equation 8 is phenomenological. Estimating $C_G(\cdot)$, $C_S(\cdot)$, and $B_{\text{homeostasis}}$ from experimental data is an open program.

17 Conclusion

We propose a boundary-first cancer framework in which malignancy is progressive loss of organism-level observability and control. The result is self-referential proliferation that is locally viable and globally destabilizing. The model links loss of contact inhibition, checkpoint failure, immune evasion, metabolic offloading, circadian disruption, and bioelectric decoupling under one boundary-logic account.

The practical value of the framework is threefold:

1. **As an organizing language:** It highlights the shared structure across seemingly different cancer mechanisms; all involve loss of cross-scale coupling and collapse into local self-reference.
2. **As a therapeutic design principle:** “Forced distinction” unifies the logic behind immunotherapy, differentiation therapy, bioelectric reprogramming, and chronotherapy. In this framing, interventions lie on a distinction-restoration continuum: some improve observability, while stronger restoration can push cells toward explicit halt states.
3. **As a source of testable hypotheses:** The framework generates predictions about circadian disruption, bioelectric markers, coherence metrics, and growth-stability dynamics that can be tested against existing and prospective data. TCGA validation across six cancer types ($n = 3,611$ tumor samples; Section 14) supports this direction: the circadian–checkpoint coupling replicates in 100% of cohorts tested (and in one external immunotherapy cohort), tumors show a transcript-level “locked” (lower-CV) clock-gene signature relative to matched normals, and patient-level survival analysis shows a significant Active Masking vs. Decoherence difference in melanoma (confirmed by PH-free RMST: +24 months at 10 years) with a directionally similar signal in lung adenocarcinoma. The survival signal is robust to threshold choice (significant at 9/11 percentile thresholds), survives immune-fraction residualization, and is captured by an independently operationalized observability index. Most other survival and stage endpoints remain non-significant after correction and are treated as bounds on the model rather than proof against all effects.

For interpretive clarity, we separate three layers: [M] metaphor (conceptual analogies such as `rec_succ`), [C] claim (structural assertions about boundary failure and observability), and [P] prediction (falsifiable hypotheses in Section 13, with multi-cancer validation in Section 14).

The Active Masking / Decoherence distinction yields hypothesis-generating therapeutic implications: checkpoint inhibitors could preferentially benefit Active Masking tumors (where the immune response is visible but vetoed), while Decoherence tumors may require differentiation therapy or antigen-restoration strategies to restore immune visibility before checkpoint blockade can be effective. This is a prospective prediction: TCGA survival analysis does not measure checkpoint-blockade response. Boundary-failure subtyping could be evaluated prospectively as a complement to existing biomarkers (PD-L1 IHC, tumor mutational burden) for immunotherapy patient selection.

Preliminary external validation in one nivolumab melanoma cohort (GSE91061, $n = 49$) replicates the circadian–checkpoint correlation but is underpowered for subtype-level response testing. Next steps are to (i) validate the Active Masking / Decoherence classification in larger independent immunotherapy cohorts with treatment-response endpoints, (ii) operationalize gap-junction and bioelectric proxies using functional assays rather than transcript-level data, (iii) test the circadian-restructuring finding in single-cell RNA-seq datasets where clock-gene heterogeneity can be resolved at cellular resolution, and (iv) pursue tumor-purity-stratified and single-cell deconvolution analyses to further resolve tumor-intrinsic from stromal contributions to the circadian–checkpoint signal. A companion repository (github.com/MosesRahnama/cancer-paper-repository) implements the tissue graph model, four therapeutic operators, TCGA extraction and analysis pipelines (six cancer types), survival analysis, immune-subtype classification, and visualization tools for reproducibility and community testing.

18 Future Research Directions

1. **Operationalizing control budget terms:** Estimating $C_G(\cdot)$, $C_S(\cdot)$, and $B_{\text{homeostasis}}$ by pairing proliferation assays with tissue-integrity and checkpoint-load metrics across tissue types.
2. **Bioelectric boundary mapping:** Applying voltage-sensitive imaging to characterize the “bioelectric boundary” of tumors *in vivo* and correlating with treatment response.
3. **Coherence biomarkers:** Developing clinical tests combining gap junction density, circadian gene coherence, and transcriptional heterogeneity into a composite tissue coherence score.
4. **Chronotherapy integration:** Testing whether circadian-aligned drug administration improves outcomes specifically in tumors with measurably disrupted clock gene expression.
5. **Differentiation therapy expansion:** Applying the “forced distinction” principle to identify differentiation-inducing agents for cancers beyond APL.
6. **Computational oncology:** Using the `rec_succ` structural analogy to develop agent-based models that predict tumor growth patterns based on termination predicate availability (p53 status, checkpoint integrity, immune visibility).

Acknowledgements

This work benefited from iterative technical review and tool-assisted drafting. All claims, interpretations, and errors are the responsibility of the author.

References

- [1] Hanahan, D., & Weinberg, R. A. (2011). Hallmarks of Cancer: The Next Generation. *Cell*, 144(5), 646–674. <https://doi.org/10.1016/j.cell.2011.02.013>
- [2] Hanahan, D. (2022). Hallmarks of Cancer: New Dimensions. *Cancer Discovery*, 12(1), 31–46. <https://doi.org/10.1158/2159-8290.CD-21-1059>
- [3] Nowell, P. C. (1976). The Clonal Evolution of Tumor Cell Populations. *Science*, 194(4260), 23–28. <https://doi.org/10.1126/science.959840>
- [4] Lineweaver, C. H., Bussey, K. J., Blackburn, A. C., & Davies, P. C. W. (2021). Cancer progression as a sequence of atavistic reversions. *BioEssays*, 43(7), e2000305. <https://doi.org/10.1002/bies.202000305>
- [5] Trigos, A. S., et al. (2017). Altered interactions between unicellular and multicellular genes drive hallmarks of transformation in a diverse range of solid tumors. *Proc. Natl. Acad. Sci. USA*, 114(25), 6406–6411. <https://doi.org/10.1073/pnas.1617743114>
- [6] Soto, A. M., & Sonnenschein, C. (2011). The tissue organization field theory of cancer: A testable replacement for the somatic mutation theory. *BioEssays*, 33(5), 332–340. <https://doi.org/10.1002/bies.201100025>
- [7] Landauer, R. (1961). Irreversibility and Heat Generation in the Computing Process. *IBM J. Res. Dev.*, 5(3), 183–191. <https://doi.org/10.1147/rd.53.0183>
- [8] Bennett, C. H. (1982). The Thermodynamics of Computation: A Review. *Int. J. Theor. Phys.*, 21(12), 905–940. <https://doi.org/10.1007/BF02084158>
- [9] Shannon, C. E. (1948). A Mathematical Theory of Communication. *Bell Syst. Tech. J.*, 27, 379–423 and 623–656.
- [10] Rahnama, M. (2026). *Thermodynamic Constraints on Measurement Events: A Boundary Framework for Classical Information*. Zenodo. <https://doi.org/10.5281/zenodo.18445561>
- [11] Turing, A. M. (1937). On Computable Numbers, with an Application to the Entscheidungsproblem. *Proc. London Math. Soc.*, s2-42(1), 230–265.
- [12] Gödel, K. (1931). Über formal unentscheidbare Sätze der Principia Mathematica und verwandter Systeme I. *Monatshefte für Mathematik und Physik*, 38(1), 173–198.
- [13] Levine, A. J., & Oren, M. (2009). The first 30 years of p53: growing ever more complex. *Nature Reviews Cancer*, 9(10), 749–758. <https://doi.org/10.1038/nrc2723>
- [14] Lane, D. P. (1992). p53, guardian of the genome. *Nature*, 358(6381), 15–16. <https://doi.org/10.1038/358015a0>

- [15] Okada, T., Lopez-Lago, M., & Giancotti, F. G. (2005). Merlin/NF-2 Mediates Contact Inhibition of Growth by Suppressing Recruitment of Rac to the Plasma Membrane. *J. Cell Biol.*, 171(2), 361–371. <https://doi.org/10.1083/jcb.200503165>
- [16] Levin, M. (2021). Bioelectric signaling: Reprogrammable circuits underlying embryogenesis, regeneration, and cancer. *Cell*, 184(6), 1971–1989. <https://doi.org/10.1016/j.cell.2021.02.034>
- [17] Levin, M. (2013). Reprogramming cells and tissue patterning via bioelectricity. *Organogenesis*, 9(3), 143–149. PMC3841289.
- [18] Zahalka, A. H., & Frenette, P. S. (2020). Nerves in cancer. *Nature Reviews Cancer*, 20(3), 143–157. <https://doi.org/10.1038/s41568-019-0237-2>
- [19] Magnon, C., et al. (2024). Autonomic nerve development and tumor growth. *Genes & Development*, 38(17–20), 802–804. <https://doi.org/10.1101/gad.352278.124>
- [20] International Agency for Research on Cancer (2019). *IARC Monographs Volume 124: Night Shift Work*. IARC, Lyon.
- [21] Schernhammer, E. S., et al. (2006). Night work and risk of breast cancer. *Epidemiology*, 17(1), 108–111. <https://doi.org/10.1097/01.ede.0000190539.03500.c1>
- [22] Finnish Twin Cohort (2023). Shift work including night shifts and breast cancer risk. *Eur. J. Epidemiol.* (2023). PMID: 36964875.
- [23] Mello, R. M., Masri, S., & Lamia, K. A. (2026). Rhythms of risk: the intersection of clocks, cancer, and chronotherapy. *J. Clin. Invest.*, 136(3), e198780. <https://doi.org/10.1172/JCI198780>
- [24] Masri, S., et al. (2016). Lung Adenocarcinoma Distally Rewires Hepatic Circadian Homeostasis. *Cell*, 165(4), 896–909. <https://doi.org/10.1016/j.cell.2016.04.039>
- [25] Grimwade, D., Mistry, A. R., Solomon, E., & Guidez, F. (2010). Acute promyelocytic leukemia: a paradigm for differentiation therapy. *Cancer Treat. Res.*, 145, 219–235.
- [26] Huang, M. E., et al. (2013). All-trans retinoic acid in acute promyelocytic leukemia. *Chin. J. Hematol.* PMC3757424.
- [27] Lin, X., Kang, K., Chen, P., et al. (2024). Regulatory mechanisms of PD-1/PD-L1 in cancers. *Molecular Cancer*, 23, 108. <https://doi.org/10.1186/s12943-024-02023-w>
- [28] Nowicki, T. S., Hu-Lieskovan, S., & Ribas, A. (2018). Mechanisms of resistance to PD-1 and PD-L1 blockade. *Cancer Journal*, 24(1), 47–53. <https://doi.org/10.1097/PPO.0000000000000303>
- [29] Warburg, O. (1956). On the Origin of Cancer Cells. *Science*, 123(3191), 309–314.

- [30] Vander Heiden, M. G., Cantley, L. C., & Thompson, C. B. (2009). Understanding the Warburg Effect. *Science*, 324(5930), 1029–1033. <https://doi.org/10.1126/science.1160809>
- [31] Pavlova, N. N., & Thompson, C. B. (2016). The Emerging Hallmarks of Cancer Metabolism. *Cell Metab.*, 23(1), 27–47.
- [32] Argilés, J. M., et al. (2024). Cancer therapy and cachexia. *J. Clin. Invest.* <https://doi.org/10.1172/JCI191934>
- [33] Cancer cachexia as multiorgan failure (2022). *Front. Cell Dev. Biol.*, 10, 960341.
- [34] Cancer connectors: Connexins, gap junctions, and communication (2018). *Front. Oncol.*, 8, 646.
- [35] The spontaneous remission of cancer: current insights and therapeutic implications (2022). *PMC*, 8271173.
- [36] Common factors among reported cases of spontaneous remission and regression of cancer (2019). *Int. J. Cancer Clin. Res.*, 6(112).
- [37] Neijssen, J., et al. (2005). Cross-presentation by intercellular peptide transfer through gap junctions. *Nature*, 434, 83–88.
- [38] Lynch, M., & Marinov, G. K. (2015). The bioenergetic costs of a gene. *Proc. Natl. Acad. Sci. USA*, 112(51), 15690–15695.
- [39] Teschendorff, A. E., & Enver, T. (2017). Single-cell entropy for accurate estimation of differentiation potency from a cell's transcriptome. *Nature Communications*, 8, 15599.
- [40] Malta, T. M., et al. (2018). Machine Learning Identifies Stemness Features Associated with Oncogenic Dedifferentiation. *Cell*, 173(2), 338–354.e15.
- [41] Curtius, K., Wright, N. A., & Graham, T. A. (2018). Evolution of Premalignant Disease. *Cold Spring Harbor Perspectives in Medicine*, 8(4), a026542. <https://doi.org/10.1101/cshperspect.a026542>
- [42] Shariff, J. A., & Zavras, A. I. (2015). Malignant Transformation Rate in Patients Presenting Oral Epithelial Dysplasia: Systematic Review and Meta-Analysis. *Journal of Oral Diseases*, 2015, 854636. <https://doi.org/10.1155/2015/854636>
- [43] Martincorena, I., & Campbell, P. J. (2015). Somatic mutation in cancer and normal cells. *Science*, 349(6255), 1483–1489. <https://doi.org/10.1126/science.aab4082>
- [44] Reynolds, S. M., et al. (2017). The ISB Cancer Genomics Cloud: A Flexible Cloud-Based Platform for Cancer Genomics Research. *Cancer Research*, 77(21), e7–e10. <https://doi.org/10.1158/0008-5472.CAN-17-0617>

- [45] Dunn, G. P., Old, L. J., & Schreiber, R. D. (2004). The Three Es of Cancer Immunoediting. *Annual Review of Immunology*, 22, 329–360. <https://doi.org/10.1146/annurev.immunol.22.012703.104803>
- [46] Schreiber, R. D., Old, L. J., & Smyth, M. J. (2011). Cancer Immunoediting: Integrating Immunity's Roles in Cancer Suppression and Promotion. *Science*, 331(6024), 1565–1570. <https://doi.org/10.1126/science.1203486>
- [47] Thorsson, V., et al. (2018). The Immune Landscape of Human Tumors. *Immunity*, 48(4), 812–830.e14. <https://doi.org/10.1016/j.immuni.2018.03.023>
- [48] Bérut, A., et al. (2012). Experimental verification of Landauer's principle linking information and thermodynamics. *Nature*, 483, 187–189. <https://doi.org/10.1038/nature10872>
- [49] Riaz, N., et al. (2017). Tumor and Microenvironment Evolution during Immunotherapy with Nivolumab. *Cell*, 171(4), 934–949.e16. <https://doi.org/10.1016/j.cell.2017.09.028>

A Code Availability and Reproducibility Assets

All executable code for this manuscript is maintained in the companion repository: <https://github.com/MosesRahnama/cancer-paper-repository>

The manuscript intentionally omits embedded Python listings to keep the paper focused on theory, evidence, and results while preserving full computational reproducibility in versioned scripts.

- **Core simulation demo:** `run_simulation.py`
- **Multi-therapy scenario runner:** `examples/run_full_scenario.py`
- **Phase-2 extracted operator sweeps:** `run_phase2_extractions.py`
- **TCGA data extraction:** `experiments/tcga/tcga_extract.py`
- **TCGA correlation analysis:** `experiments/tcga/tcga_analysis.py`
- **Multi-cancer expansion:** `experiments/tcga/tcga_multicancer.py`
- **Tumor vs. normal comparison:** `experiments/tcga/tcga_tumor_normal.py`
- **Immune subtype classification:** `experiments/tcga/tcga_immune_subtype.py`
- **Survival analysis:** `experiments/tcga/tcga_survival.py`
- **Stage-stratified analysis:** `experiments/tcga/tcga_stage_analysis.py`
- **Threshold sensitivity sweep:** `experiments/tcga/sensitivity_threshold_sweep.py`
- **RMST survival analysis:** `experiments/tcga/sensitivity_rmst.py`
- **Immune residualization:** `experiments/tcga/sensitivity_immune_residualization.py`
- **Composite observability index:** `experiments/tcga/composite_observability_index.py`
- **External validation (GSE91061):** `experiments/tcga/run_external_validation.py`
- **Generated outputs:** `results/` (JSON + figures used in this manuscript)